

Equilibrium of Free Surfaces and Nanoparticles in Self-Consistent Field Theory of Block Copolymers

Daniil Bochkov,^{*,†} Ivana Bagaric,[‡] Gadiel Ouaknin,[†] and Frédéric Gibou^{†,¶}

[†]*Department of Mechanical Engineering, University of California, Santa Barbara, Santa Barbara, CA, 93106*

[‡]*Institute of Fluid Dynamics, Swiss Federal Institute of Technology Zurich, Zurich, Switzerland*

[¶]*Department of Computer Science, University of California, Santa Barbara, Santa Barbara, CA, 93106*

E-mail: bochkov.ds@gmail.com

Abstract

This work presents a general and unified theory describing block copolymer self-assembly in the presence of free surfaces and nanoparticles in the context of Self-Consistent Field Theory. Specifically, the derived theory applies to free and tethered polymer chains, nanoparticles of any shape, arbitrary non-uniform surface energies and grafting densities, and takes into account a possible formation of triple-junction points (e.g., polymer-air-substrate). One of the main ingredients of the proposed theory is a simple procedure for a consistent imposition of boundary conditions on surfaces with non-zero surface energies and/or non-zero grafting densities that results in singularity-free pressure-like fields, which is crucial for the calculation of forces. The generality of the theory is demonstrated using several representative examples such as the meniscus

formation in the graphoepitaxy and the co-assembly of “polarized” nano-rods and diblock copolymer melts.

1 Introduction

Self-Consistent Field Theory^{1,2} (SCFT) is a powerful framework that has become a standard approach for modeling block copolymer (BCP) self-assembly. In its standard form, SCFT is suitable for investigating periodic (bulk) morphologies of self-assembling BCPs or in static confinements. However, in certain situations, such as in the presence of polymer-air interface and/or nanoparticles, the confining boundaries are free to move and in fact must be considered as part of the solution.

The importance of simulating free surface block copolymer melts comes from the fact that it is not uncommon in practical applications for the polymer material to be exposed to a gaseous or liquid phase. Free surfaces provide a channel for releasing internal stresses of polymer melts. This can lead not only to alterations in spatial dimensions of self-assembled features, but to the potential relaxation into a different, more energetically stable morphology. For example, besides the meniscus formation near confining walls, this can also lead to the formation of unique free surface features of block copolymers such as holes, islands, and terraces.^{3,4} The simulation of block copolymer free surfaces is challenging due to the two-way coupling between the free surface and the internal polymer morphology. Within the SCFT framework, free polymer surfaces are typically modeled by introducing into the system an additional chemical species that play the role of the air.⁵⁻⁷ While being simple and straightforward to implement, this approach is not free of caveats. Among them is the fact that only relatively low interaction strengths between dissimilar species can be used in the SCFT for numerical calculations to remain stable. This leads to the inability to impose physically high incompatibility between the polymer material and the surrounding air as well as to a smeared-out polymer-air interface. In Ouaknin *et al.*,⁸ a conceptually different

framework has been proposed, where the polymer-air interface is treated in a sharp fashion and its governing equations are derived based on the PDE-constrained shape sensitivity analysis. However, results in Ouaknin *et al.*⁸ are limited to neutral polymer-air interfaces due to the well-known inconsistency within the SCFT to model selectively attractive/repulsive boundaries.²

Mixing of BCPs and nanoparticles constitutes a promising avenue for the creation of functional materials and advanced polymer self-assembly applications.⁹ Similar to the case of free polymer surfaces, the theoretical description of these systems is complicated by two-way couplings: on the one hand, the self-assembling polymer structures guide the placement of nanoparticles but, on the other hand, the presence of nanoparticles influence the resulting polymer morphologies. The problem of co-assembly of BCPs and nanoparticles in the SCFT framework has been approached from explicit and implicit perspectives. In the former case, each nanoparticle in the system is described explicitly while in the latter case, the distribution of nanoparticles is described in terms of density fields. Each framework has its own advantages: the first methodology allows for a straightforward incorporation of such features as excluded volume effects, arbitrary shapes of particles, complex particle-particle interactions; the second methodology is more efficient at obtaining statistical information about particles configurations. The explicit approach was employed in the hybrid particle-field method proposed in Sides *et al.*,¹⁰ in which nanoparticles were modeled by the so-called cavity function that represents a gradual transition between polymer and particle's material and the relaxation of nanoparticles towards the equilibrium state is accomplished using an approximate derivatives of the system's energy with respect to the particles' positions. Among implicit approaches are the hybrid SCFT-DFT method proposed in Thompson *et al.*¹¹ and the field-theoretic method described in Koski *et al.*¹²

In this work we derive a generalized and unified theory in the context of SCFT describing equilibrium of polymer free surfaces and submerged nanoparticles extending the ideas introduced in Ouaknin *et al.*⁸ The interfaces between polymer melt and surrounding mate-

rial are considered to be sharp. Surface energies and surface grafting densities are modeled in a unified consistent approach that results in pressure-like fields free of singularities near domain boundaries. The theory is derived for an arbitrary mixture of linear BCP chains containing both free and tethered polymer chains in the case of arbitrary non-uniform surface energies and grafting densities. The shapes of substrate and nanoparticles are considered to be arbitrary as well and three-phase (e.g., polymer-air-substrate) triple junctions are explicitly taken into account. The theory is implemented numerically in the Level-Set Method framework along the lines of Ouaknin *et al.*,¹³ validated using benchmark tests, and applied to model the meniscus formation in graphoepitaxy and the co-assembly of nano-rods and diblock copolymer melts.

The rest of this manuscript is organized as follows. Section 2 presents a consistent approach for imposing arbitrary surface energies and grafting densities for incompressible BCP melts in the SCFT framework. In sections 3 we derive the expressions for forces acting on polymer free surface and submerged nanoparticles. In section 4, we briefly discuss the numerical implementation used in this work. In section 5 we present a number of examples demonstrating the capabilities of the proposed methods. Finally, section 6 draws conclusions and discusses future research directions.

2 A consistent approach for imposing arbitrary surface energies and grafting densities in SCFT

Let us consider an incompressible mixture of n linear block copolymer chains composed of two chemical species denoted as A and B in a region Ω with boundary Γ as pictured in Figure 1. Specifically, we assume that there exist M types (e.g., AB, ABA, BABA, etc) of polymer chains and that the fraction of chains belonging to a particular type is given by ϕ_α , $\alpha = 1, \dots, M$. The length of chains for a given type α is given by $l_\alpha N$, where N is a representative number of statistical segments in polymer chains. The individual shapes of

polymer chains are parametrized by the contour variable s and are denoted as $\mathbf{r}_{\alpha,j} = \mathbf{r}_{\alpha,j}(s)$, such that $s \in [0, l_\alpha]$ for $\alpha \in [1, M]$, $j \in [1, \phi_\alpha n]$. The precise composition of chains for a given type α is given by function $\zeta_\alpha(s)$ taking values -1 and 1 , such that $\zeta_\alpha(s) = -1$ corresponds to an A segment at location s and $\zeta_\alpha(s) = 1$ corresponds to a B segment at location s . We assume that fraction G_α of polymer chains of type α are grafted with density $g_\alpha(\mathbf{r})$ onto domain boundary Γ . We also denote the surface energy (potentially, nonuniform) of species A and B on boundary Γ as $\gamma_A = \gamma_A(\mathbf{r})$ and $\gamma_B = \gamma_B(\mathbf{r})$, correspondingly. Furthermore, as a common practice it is assumed that A and B statistical segments have equal volumes v_0 . In the following we, first, briefly outline the derivation of a mean-field approximation for this system (see, e.g., Fredrickson² for a more detailed discussion) and then describe a general procedure to ensure non-singular behavior of the pressure-like chemical field.

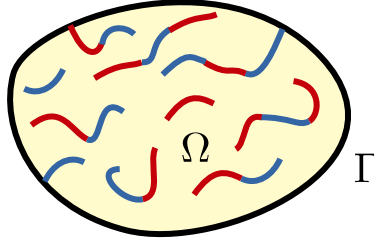


Figure 1: Problem geometry and notation used in section 2.

The total stretching energy of polymer chains can be written as:

$$U_0 = \beta^{-1} \sum_{\alpha=1}^M \sum_{j=1}^{n_\alpha} \int_0^{l_\alpha} \frac{1}{4} \left| \frac{d\mathbf{r}_{\alpha,j}(s)}{ds} \right|^2 ds$$

where $\beta = \frac{1}{k_B T}$. Note that spatial quantities are measured in units of a representative gyration radius $R_g = b\sqrt{\frac{N}{6}}$, where b is the statistical length of a single polymer bead (assumed equal for all beads in a polymer chain).

The interaction energy between dissimilar chemical blocks is taken into account through a Flory-Huggins effective interaction parameter χ_{AB} :

$$U_1 = \beta^{-1} \frac{1}{v_0} \chi_{AB} \int_{\Omega} \hat{\rho}_A \hat{\rho}_B d\mathbf{r},$$

where the microscopic number concentrations, that is, fraction of segments at any point, are given by:

$$\hat{\rho}_A = v_0 N \sum_{\alpha=1}^M \sum_{j=1}^{n_\alpha} \int_0^{l_\alpha} H(-\zeta_\alpha(s)) \delta(\mathbf{r} - \mathbf{r}_j(s)) ds$$

$$\hat{\rho}_B = v_0 N \sum_{\alpha=1}^M \sum_{j=1}^{n_\alpha} \int_0^{l_\alpha} H(\zeta_\alpha(s)) \delta(\mathbf{r} - \mathbf{r}_j(s)) ds,$$

where $H(x)$ is the Heaviside step function.

Finally, the total surface energy of the polymer melt can be expressed as:

$$U_2 = \int_{\Gamma} (\gamma_A \hat{\rho}_A + \gamma_B \hat{\rho}_B) d\mathbf{r} = \int_{\Omega} (\gamma_A \hat{\rho}_A + \gamma_B \hat{\rho}_B) \delta_{\Gamma} d\mathbf{r},$$

where it is assumed that the local surface energy of the polymer material is equal to a weighted averaged of surface energies of A and B species, and where δ_{Γ} represents the surface delta function associated with domain boundary Γ .

Taking into account stretching, interaction, and surface energies the total energy of the system U can be expressed as:

$$U = U_0 + U_1 + U_2$$

Using the Hubbard-Stratonovich transformation, the canonical partition function can be expressed as:

$$\mathcal{Z}_C = \mathcal{Z}_0 \iint \exp(-H[\mu_+, \mu_-]) \mathcal{D}\mu_+ \mathcal{D}\mu_-,$$

where \mathcal{Z}_0 denotes the ideal gas partition function, μ_+ and μ_- are fluctuating pressure-like

and exchange-like potential fields, and the effective Hamiltonian H is given by:

$$\begin{aligned} \frac{H}{n} = \frac{1}{V} \int_{\Omega} \left(\frac{\mu_-^2}{\chi_{AB} N} - \mu_+ \right) d\mathbf{r} - \sum_{\alpha=1}^M (1 - G_{\alpha}) \varphi_{\alpha} \log(Q_{\alpha}^f[\mu_-, \mu_+]) \\ - \sum_{\alpha=1}^M G_{\alpha} \varphi_{\alpha} \int_{\Gamma} g_{\alpha}(\mathbf{r}) \log(Q_{\alpha}^t[\mathbf{r}; \mu_-, \mu_+]) d\mathbf{r}. \end{aligned}$$

The single-chain partition functions of a free chain Q_{α}^f and a tethered one Q_{α}^t can be computed from the respective chain propagators $q_{\alpha}^f = q_{\alpha}^f(s, \mathbf{r})$ and $q_{\alpha}^t = q_{\alpha}^t(s, \mathbf{r})$ as:¹⁴

$$Q_{\alpha}^f = \frac{1}{V} \int_{\Omega} q_{\alpha}^f(l_{\alpha}, \mathbf{r}) d\mathbf{r} \quad \text{and} \quad Q_{\alpha}^t(\mathbf{r}) = q_{\alpha}^t(l_{\alpha}, \mathbf{r}) \quad (1)$$

Chain propagators q_{α}^f and q_{α}^t satisfy the so-called modified diffusion equations which, in this particular case of tethered and untethered polymer chains having the same composition, are identical. Thus, we denote both of them by a single symbol $q_{\alpha} = q_{\alpha}^f = q_{\alpha}^t$ where:

$$\begin{cases} \partial_s q_{\alpha} + (\mu_{\alpha}(s) + \eta \gamma_{\alpha}(s) \delta_{\Gamma}) q_{\alpha} = \nabla^2 q_{\alpha}, & \mathbf{r} \in \Omega, \quad 0 < s \leq l_{\alpha}, \\ \partial_{\mathbf{n}} q_{\alpha} = 0, & \mathbf{r} \in \Gamma, \quad 0 < s \leq l_{\alpha}, \\ q_{\alpha} = 1, & \mathbf{r} \in \Omega, \quad s = 0 \end{cases} \quad (2)$$

where $\eta = \frac{Nv_0}{R_g} \frac{1}{k_B T}$ and

$$\begin{aligned} \mu_{\alpha}(s) &= \mu_+ + \zeta_{\alpha}(s) \mu_- \\ \gamma_{\alpha}(s) &= \frac{\gamma_B + \gamma_A}{2} + \zeta_{\alpha}(s) \frac{\gamma_B - \gamma_A}{2} \end{aligned}$$

The total fractions of block A and B at any point in space can be computed as:

$$\rho_A(\mathbf{r}) = \sum_{\alpha=1}^M \varphi_{\alpha} \int_0^{l_{\alpha}} H(-\zeta_{\alpha}(s)) q_{\alpha}(s, \mathbf{r}) \hat{q}_{\alpha}(s, \mathbf{r}) ds, \quad (3)$$

$$\rho_B(\mathbf{r}) = \sum_{\alpha=1}^M \varphi_{\alpha} \int_0^{l_{\alpha}} H(\zeta_{\alpha}(s)) q_{\alpha}(s, \mathbf{r}) \hat{q}_{\alpha}(s, \mathbf{r}) ds, \quad (4)$$

where $\hat{q}_\alpha = (1 - G_\alpha) \frac{\hat{q}_\alpha^f}{Q^f} + G_\alpha V \hat{q}_\alpha^t$ is a weighted sum of the so-called *complimentary chain propagators* for free and tethered chains, \hat{q}_α^f and \hat{q}_α^t , of type α and satisfies:

$$\begin{cases} -\partial_s \hat{q}_\alpha + (\mu_\alpha(s) + \eta \gamma_\alpha(s) \delta_\Gamma) \hat{q}_\alpha = \nabla^2 \hat{q}_\alpha, & \mathbf{r} \in \Omega, \quad 0 \leq s < l_\alpha, \\ \partial_n \hat{q}_\alpha = 0, & \mathbf{r} \in \Gamma, \quad 0 \leq s < l_\alpha, \\ \hat{q}_\alpha = \hat{q}_\alpha^0, & \mathbf{r} \in \Omega, \quad s = l_\alpha. \end{cases} \quad (5)$$

The expression for initial conditions in the above PDE $\hat{q}_\alpha^0 = \frac{1-G_\alpha}{Q^f} + \frac{G_\alpha g_\alpha(\mathbf{r})}{Q^t} V \delta_\Gamma$ contains a uniform part $\frac{1-G_\alpha}{Q^f}$, corresponding to free chains originating at any point with equal probability, and a singular one $\frac{G_\alpha g_\alpha(\mathbf{r})}{Q^t} V \delta_\Gamma$, corresponding to tethered chains originating only at grafting surfaces and according to grafting density $g_\alpha(\mathbf{r})$.

A mean-field approximation for this system is obtained by accounting only for instances of fields $\mu_+ = \mu_+^*$ and $\mu_- = \mu_-^*$ that have the largest contribution in \mathcal{Z}_C , that is:

$$\mathcal{Z}_C \approx \exp(-H[\mu_+^*, \mu_-^*]),$$

where

$$\frac{\delta H}{\delta \mu_+}[\mu_+^*, \mu_-^*] = 0 \quad \text{and} \quad \frac{\delta H}{\delta \mu_-}[\mu_+^*, \mu_-^*] = 0. \quad (6)$$

This results in the following so-called SCFT equations:

$$\rho_A + \rho_B = 1, \quad (7)$$

$$\rho_A - \rho_B = \frac{2\mu_-^*}{\chi N}, \quad (8)$$

Note that equations (2) and (5) involve delta-like potentials which may be difficult to deal with from the numerical point of view. Some of the previous works avoided this issue by approximating the delta-like potential by a smooth function.¹⁵ Such an approach, however, introduces an artificial scale over which the delta function is smoothed. Alternatively, it can be shown (see Appendix A) that the diffusion equations (2) and (5) are equivalent to:

$$\begin{cases} \partial_s q_\alpha + \mu_\alpha(s)q_\alpha = \nabla^2 q_\alpha, & \mathbf{r} \in \Omega, \quad 0 < s \leq l_\alpha, \\ \partial_{\mathbf{n}} q_\alpha + \eta\gamma_\alpha(s)q_\alpha = 0, & \mathbf{r} \in \Gamma, \quad 0 < s \leq l_\alpha, \\ q_\alpha = 1, & \mathbf{r} \in \Omega, \quad s = 0 \end{cases} \quad (9)$$

and

$$\begin{cases} -\partial_s \hat{q}_\alpha + \mu_\alpha(s)\hat{q}_\alpha = \nabla^2 \hat{q}_\alpha, & \mathbf{r} \in \Omega, \quad 0 \leq s < l_\alpha, \\ \partial_{\mathbf{n}} \hat{q}_\alpha + \eta\gamma_\alpha(s)\hat{q}_\alpha = 0, & \mathbf{r} \in \Gamma, \quad 0 \leq s < l_\alpha, \\ \hat{q}_\alpha = \hat{q}_\alpha^0, & \mathbf{r} \in \Omega, \quad s = l_\alpha \end{cases} \quad (10)$$

where the surface energy terms now enter as a Robin (mixed) boundary conditions (this form can also be obtained directly from fully-fluctuating theory). This formulation is significantly more amenable to standard numerical methods without additional approximations, the only remaining non-smooth feature of the above equations is the delta-like distribution in the initial conditions for \hat{q}_α . However, given the diffusive nature of the PDE, such a singular feature does not persist, in fact the solution is infinitely smooth for $s > 0$, thus only the initial condition needs a special treatment. Specifically, in this work, we employ a finite volume method in which volumetric integration of the delta-like distribution leads to a well-defined surface integral as discussed in later sections.

While the solution to the forward and backward diffusion equations (9)-(10) is expected to produce smooth quantities, it turns out that solving the entire system of the SCFT equation might still produce a singular behavior.^{2,16,17} Mathematically, this is due to the fact that Robin boundary conditions representing surface energies and initial conditions for \hat{q} representing tethered ends are not consistent with equation (7) representing the incompressibility of the system. In order to see this more clearly, we, first, note that equation (10) can be equivalently written as

$$\left\{ \begin{array}{ll} -\partial_s \hat{q}_\alpha + (\mu_\alpha(s) + \eta \gamma_\alpha(s) \delta_\Gamma) \hat{q}_\alpha = \nabla^2 \hat{q}_\alpha, & \mathbf{r} \in \Omega, \quad 0 \leq s < l_\alpha, \\ \partial_{\mathbf{n}} \hat{q}_\alpha + \eta \gamma_\alpha(s) \hat{q}_\alpha = \frac{G_\alpha g_\alpha(\mathbf{r})}{Q^t} V \delta(s - l_\alpha), & \mathbf{r} \in \Gamma, \quad 0 \leq s < l_\alpha, \\ \hat{q}_\alpha = \frac{1 - G_\alpha}{Q^f}, & \mathbf{r} \in \Omega, \quad s = l_\alpha \end{array} \right. \quad (11)$$

where now the inhomogeneity of Robin boundary conditions model the effect of tethered chain ends. Now, taking the derivative of (3) on the domain boundary in the normal direction and using the boundary conditions from (9) and (10) one obtains:

$$\partial_{\mathbf{n}} (\rho_A + \rho_B) = -2\eta (\gamma_A \rho_A + \gamma_B \rho_B) + V \sum_{\alpha=1}^M G_\alpha \varphi_\alpha g_\alpha(\mathbf{r}),$$

while differentiating the incompressibility equation (7) leads to:

$$\partial_{\mathbf{n}} (\rho_A + \rho_B) = 0.$$

It is clear that the two results are inconsistent whenever the surface potentials are nonzero ($\gamma_A \neq 0$ and/or $\gamma_B \neq 0$) or tethered polymer chains are present ($g_\alpha(\mathbf{r}) \neq 0$). Attempting to solve the entire system of SCFT equations with chain propagators satisfying the above diffusion equations produces pressure fields with a singular behavior near domain boundaries. Physically, one can interpret this behavior in the following way: crowding of tethered polymer chain ends or non-zero surface potentials results in emerging of a compressing force which is acting on an incompressible substance.

While for certain applications such a singular behavior does not have an adverse effect, it is crucial to have well-defined values of the pressure field for modeling polymer-air and polymer-particle interactions. We now show that the described inconsistency is only apparent and can be completely removed.

Using, again, the results of A, we can write the diffusion equations (9) and (10) in yet another equivalent form:

$$\begin{cases} \partial_s q_\alpha + (\mu_\alpha(s) + \eta\gamma_c) q_\alpha = \nabla^2 q_\alpha, & \mathbf{r} \in \Omega, \quad 0 < s \leq l_\alpha, \\ \partial_n q_\alpha + \eta(\gamma_\alpha(s) - \gamma_c) q_\alpha = 0, & \mathbf{r} \in \Gamma, \quad 0 < s \leq l_\alpha, \\ q_\alpha = 1, & \mathbf{r} \in \Omega, \quad s = 0 \end{cases} \quad (12)$$

and

$$\begin{cases} -\partial_s \hat{q}_\alpha + (\mu_\alpha(s) + \eta\gamma_c) \hat{q}_\alpha = \nabla^2 \hat{q}_\alpha, & \mathbf{r} \in \Omega, \quad 0 \leq s < l_\alpha, \\ \partial_n \hat{q}_\alpha + \eta(\gamma_\alpha(s) - \gamma_c) \hat{q}_\alpha = \frac{G_\alpha g_\alpha(\mathbf{r})}{Q^t} V \delta(s - l_\alpha), & \mathbf{r} \in \Gamma, \quad 0 \leq s < l_\alpha, \\ \hat{q}_\alpha = \frac{1 - G_\alpha}{Q^f}, & \mathbf{r} \in \Omega, \quad s = l_\alpha, \end{cases} \quad (13)$$

where we added and subtracted an arbitrary function $\gamma_c = \gamma_c(\mathbf{r})$ defined on the domain's boundary Γ from the surface energy terms of the boundary conditions. Having this freedom in choosing the exact form of γ_c allows one to ensure that the boundary conditions in equations (12) and (13) are consistent with the incompressibility equation (7). Indeed, taking the normal derivative of the total density on the domain boundary and equating it to zero leads to the following equation for γ_c :

$$-2\eta((\gamma_A - \gamma_c)\rho_A + (\gamma_B - \gamma_c)\rho_B) + V \sum_{\alpha=1}^M G_\alpha \varphi_\alpha g_\alpha(\mathbf{r}) = 0,$$

from which it follows that if γ_c is chosen as:

$$\gamma_c = \frac{(\gamma_A \rho_A + \gamma_B \rho_B) - \frac{1}{2}\eta^{-1}V \sum_{\alpha=1}^M G_\alpha \varphi_\alpha g_\alpha(\mathbf{r})}{\rho_A + \rho_B},$$

then there is no inconsistency between the incompressibility equation (7) and the boundary conditions in (12) and (13).

Finally, redefining the pressure field as $\mu_+ \rightarrow \mu_+ - \eta\gamma_c\delta_\Gamma$, or in other words, explicitly subtracting from it the singular part, one arrives to the following equations for chain propagators:

$$\begin{cases} \partial_s q_\alpha + \mu_\alpha(s) q_\alpha = \nabla^2 q_\alpha, & \mathbf{r} \in \Omega, \quad 0 < s \leq l_\alpha, \\ \partial_n q_\alpha + \eta(\gamma_\alpha(s) - \gamma_c) q_\alpha = 0, & \mathbf{r} \in \Gamma, \quad 0 < s \leq l_\alpha, \\ q_\alpha = 1, & \mathbf{r} \in \Omega, \quad s = 0 \end{cases} \quad (14)$$

and

$$\begin{cases} -\partial_s \hat{q}_\alpha + \mu_\alpha(s) \hat{q}_\alpha = \nabla^2 \hat{q}_\alpha, & \mathbf{r} \in \Omega, \quad 0 \leq s < l_\alpha, \\ \partial_n \hat{q}_\alpha + \eta(\gamma_\alpha(s) - \gamma_c) \hat{q}_\alpha = \frac{G_\alpha g_\alpha(\mathbf{r})}{Q^t} V \delta(s - l_\alpha), & \mathbf{r} \in \Gamma, \quad 0 \leq s < l_\alpha, \\ \hat{q}_\alpha = \frac{1 - G_\alpha}{Q^f}, & \mathbf{r} \in \Omega, \quad s = l_\alpha, \end{cases} \quad (15)$$

and the system's energy:

$$\begin{aligned} \frac{H}{n} = & \frac{1}{V} \int_{\Omega} \left(\frac{\mu_-^2}{\chi_{AB} N} - \mu_+ \right) d\mathbf{r} + \eta \frac{1}{V} \int_{\Gamma} \gamma_c d\Gamma \\ & - \sum_{\alpha=1}^M \varphi_\alpha \left[(1 - G_\alpha) \log(Q_\alpha[\mu_-, \mu_+]) + G_\alpha \int_{\Gamma} g_\alpha(\mathbf{r}) \log(Q_\alpha[\mathbf{r}; \mu_-, \mu_+]) d\mathbf{r} \right], \end{aligned} \quad (16)$$

which are completely free of inconsistencies. From this result, γ_c can be interpreted as the effective surface energy of the polymer material. Note that it contains two contributions: one from the nominal surface energies of A and B blocks ($\frac{\gamma_A \rho_A + \gamma_B \rho_B}{\rho_A + \rho_B}$), and the second one due to tethered polymer ends ($-\frac{\frac{1}{2} \eta^{-1} V \sum_{\alpha=1}^M \varphi_\alpha G_\alpha g_\alpha(\mathbf{r})}{\rho_A + \rho_B}$).

Remark. We note that in Matsen *et al.*¹⁶ a similar approach was proposed to subtract off a singularity in the pressure field. However, singularities only due to tethered chain ends on planar geometries were considered. The magnitude of the singularity was deduced from an in-depth analysis of the Strong Segregation Theory. The described above derivation offers a simpler and unified approach for computing the magnitude of pressure singularities which is straightforward to apply in a general multidimensional setting for domains of arbitrary shapes.

Remark. In the numerical experiments, we characterize the strength of surface en-

ergy using the expression for interfacial tension of a symmetric polymer-polymer interface estimated in the case of strong segregation:²

$$\gamma = \frac{1}{\eta} \sqrt{\chi N}.$$

Imposing surface energies using the above formula in terms of χN allows straightforward comparison with A - B interaction strength $\chi_{AB}N$.

2.1 Solving the SCFT equations for μ_+^* and μ_-^*

The common approach for obtaining a saddle point $(\mu_+, \mu_-) = (\mu_+^*, \mu_-^*)$ of the Hamiltonian H is to start from some initial guess (seed) $(\mu_+, \mu_-) = (\mu_+^{(0)}, \mu_-^{(0)})$ and to iteratively evolve the fields (μ_+, μ_-) in the steepest descent/ascent directions until a saddle point is reached within a specified tolerance ε_{tol} , that is, given values at the k th iteration fields at the $(k+1)$ th iteration are updated as:

$$\begin{aligned} \mu_+^{(k+1)} &= \mu_+^{(k)} + \lambda_+ \frac{\delta H}{\delta \mu_+}[\mu_+^{(k)}, \mu_-^{(k)}] = \mu_+^{(k)} + \lambda_+ \left(\rho_A^{(k)} + \rho_B^{(k)} - 1 \right), \\ \mu_-^{(k+1)} &= \mu_-^{(k)} - \lambda_- \frac{\delta H}{\delta \mu_-}[\mu_+^{(k)}, \mu_-^{(k)}] = \mu_-^{(k)} - \lambda_- \left(\frac{2\mu_-^{(k)}}{\chi_{AB}N} - \rho_A^{(k)} + \rho_B^{(k)} \right), \end{aligned} \quad (17)$$

where λ_+ and λ_- are step sizes in moving along steepest descent/ascent directions (typically, taken as $\lambda_+ = \lambda_- = 1$), and iterations are terminated once

$$\frac{1}{V} \sqrt{\int_{\Omega} \left(\frac{\delta H}{\delta \mu_+} \right)^2 d\mathbf{r}} < \varepsilon_{\text{tol}} \quad \text{and} \quad \frac{1}{V} \sqrt{\int_{\Omega} \left(\frac{\delta H}{\delta \mu_-} \right)^2 d\mathbf{r}} < \varepsilon_{\text{tol}}. \quad (18)$$

The solution of the proposed modified system of the SCFT equations accounting for surface energies is further complicated by the presence of terms depending on γ_c , which in turn is a function of the local densities ρ_A and ρ_B . One possible strategy could be simply to recalculate the values for γ_c every few fields updates μ_- and μ_+ . However, we observed that this approach still results in numerical artifacts in the pressure field μ_+ . This seems to be

linked to the fact that in such a case, the density fields ρ_A and ρ_B generally do not satisfy the condition $\partial_{\mathbf{n}}(\rho_A + \rho_B) = 0$ during such iterations. Once the pressure field is polluted with features of small enough scale they persist for extremely long times. Our experience suggested that a better strategy is to iteratively find γ_c that satisfies $\partial_{\mathbf{n}}(\rho_A + \rho_B) = 0$ (we observed that a small number of iterations $n_\gamma = 2-4$ is sufficient) before every update of fields μ_- and μ_+ . The overall procedure for solving modified system of SCFT equations can be summarized as follows:

1. Set a desired seed for $\mu_-^{(0)}$ and $\mu_+^{(0)} = 0$.
2. Iterate in k until conditions (18) are satisfied:
 - (a) Iterate n_γ times:
 - i. Set $\gamma_c = \frac{(\gamma_A \rho_A + \gamma_B \rho_B) - \frac{1}{2} \eta^{-1} V \sum_{\alpha=1}^M \varphi_\alpha G_\alpha g_\alpha(\mathbf{r})}{\rho_A + \rho_B}$
 - ii. Solve diffusion equations (14) and (15)
 - iii. Compute density fields according to (3)
 - (b) Compute $\mu_+^{(k+1)}$ and $\mu_-^{(k+1)}$ using (17)

3 Forces acting on free surfaces and nanoparticles

Without loss of generality, let us now consider a polymer droplet containing a nanoparticle of arbitrary shape on a (possibly curved) substrate as illustrated in figure 2. The generalizations to the case of multiple particles is straightforward. For convenience, we refer to the surrounding substance as “air”, however it represents any gaseous or liquid non-solvent material. Similarly, the term “substrate” stand for a body partially submerged in the polymer material, which could be a stationary substrate or a movable partially sunk nanoparticle. As in previous section, we denote the region occupied by the polymer material as Ω . The boundary of this region, denoted as Γ , consists of the polymer-wall interface Γ_w , polymer-air interface Γ_a , and polymer-particle interface Γ_p , that is, $\Gamma = \Gamma_w \cup \Gamma_a \cup \Gamma_p$. We denote the

surface energy of the A and B blocks on these interfaces as γ_{wA}, γ_{wB} ; γ_{aA}, γ_{aB} ; and γ_{pA}, γ_{pB} ; correspondingly. The surface energy of the air-wall interface is denoted as γ_{aw} . The air related surface energies, γ_{aA}, γ_{aB} , and γ_{aw} , are assumed to be constants, while the polymer-wall and polymer-particle surface energies can be spatially variable quantities $\gamma_{wA} = \gamma_{wA}(\mathbf{r})$, $\gamma_{wB} = \gamma_{wB}(\mathbf{r})$, $\gamma_{pA} = \gamma_{pA}(\mathbf{r})$, $\gamma_{pB} = \gamma_{pB}(\mathbf{r})$. We assume that polymer chain can only be grafted onto the nanoparticle, that is, $g_\alpha(\mathbf{x}) = 0$ for $\mathbf{x} \notin \Gamma_p$.

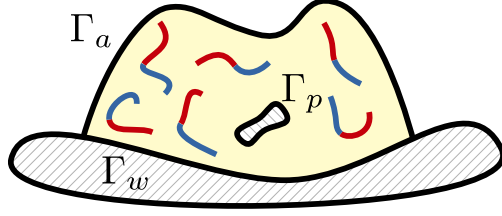


Figure 2: Problem geometry and notation used in section 3.

Given the results of the previous section, the energy of such a system per polymer chain can be expressed as:

$$\begin{aligned} \frac{HV}{n} = & \int_{\Omega} \left(\frac{\mu_-^2}{\chi_{AB}N} - \mu_+ \right) d\mathbf{r} - V \sum_{\alpha=1}^M \varphi_\alpha \log(Q_\alpha[\mu_-, \mu_+]) \\ & - V \sum_{\alpha=1}^M \varphi_\alpha \int_{\Gamma_p} g_\alpha(\mathbf{r}) \log(Q_\alpha[\mathbf{r}; \mu_-, \mu_+]) d\mathbf{r} + \eta \sum_{\nu=a,p,w} \int_{\Gamma_\nu} \gamma_{\nu,c} d\Gamma - \eta \int_{\Gamma_a} \gamma_{aw} d\Gamma, \end{aligned}$$

where

$$\begin{aligned} \gamma_{w,c} &= \frac{(\gamma_{wA}\rho_A + \gamma_{wB}\rho_B)}{\rho_A + \rho_B}, \\ \gamma_{p,c} &= \frac{(\gamma_{pA}\rho_A + \gamma_{pB}\rho_B) - \frac{1}{2}\eta^{-1}V \sum_{\alpha=1}^M \varphi_\alpha G_\alpha g_\alpha(\mathbf{r})}{\rho_A + \rho_B}, \\ \gamma_{a,c} &= \frac{(\gamma_{aA}\rho_A + \gamma_{aB}\rho_B)}{\rho_A + \rho_B}, \end{aligned}$$

single chain partition functions Q_f and Q_t are given by (1) and where chain propagators q_f and q_t satisfy the modified diffusion equations (14) provided $\Gamma = \Gamma_a \cup \Gamma_w \cup \Gamma_p$ and

$$\gamma_A = \begin{cases} \gamma_{aA}, & \mathbf{r} \in \Gamma_a, \\ \gamma_{wA}, & \mathbf{r} \in \Gamma_w, \\ \gamma_{pA}, & \mathbf{r} \in \Gamma_p, \end{cases} \quad \gamma_B = \begin{cases} \gamma_{aB}, & \mathbf{r} \in \Gamma_a, \\ \gamma_{wB}, & \mathbf{r} \in \Gamma_w, \\ \gamma_{pB}, & \mathbf{r} \in \Gamma_p. \end{cases}$$

To derive expressions for the forces acting on the free surface and the nanoparticle, we consider a situation in which the free surface is being deformed with an arbitrary normal velocity v_n , the nanoparticle is moving with translational and rotational velocities \mathbf{v}_p and $\boldsymbol{\omega}_p$, and the substrate¹ is moving with translational and rotational velocities \mathbf{v}_w and $\boldsymbol{\omega}_w$ in fictitious time τ as depicted in Figure 3, and compute analytically the derivative of the system's energy with respect to τ . In doing so, one has to take into account three effects that

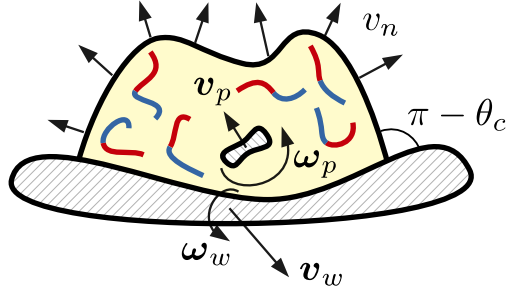


Figure 3: Deformation of free surface in normal velocity field v_n .

an evolving problem geometry incurs: (1) changes in domains of integration (assuming all integrands are independent of τ); (2) changes in chain propagators $q_f = q_f(\tau)$ and $q_t = q_t(\tau)$ (assuming μ_- and μ_+ are independent of τ); (3) changes in the overall SCFT solutions represented by fields $\mu_- = \mu_-(\tau)$ and $\mu_+ = \mu_+(\tau)$. First, we note that due to the nature of the problem, specifically, that μ_- and μ_+ satisfy saddle-point conditions, the contribution of the third effect in the change of system's energy is zero. Indeed, by applying the chain rule one obtains:

¹While the motion of the substrate does not correspond to a practically relevant situation, it allows to apply the derived below theory in the case when the term “substrate” represents a partially submerged nanoparticle.

$$\frac{dH}{d\tau} = \int_{\Omega} \underbrace{\frac{\delta H}{\delta \mu_+}}_{=0} \frac{d\mu_+}{d\tau} d\mathbf{r} + \int_{\Omega} \underbrace{\frac{\delta H}{\delta \mu_-}}_{=0} \frac{d\mu_-}{d\tau} d\mathbf{r} + \left. \frac{dH}{d\tau} \right|_{\mu=\text{const}} = \left. \frac{dH}{d\tau} \right|_{\mu=\text{const}}$$

This means that only the first two effects need to be taken into account while deriving the derivative of system's energy with respect to τ , which simplifies the task significantly. To take into account the second effect we use a Lagrangian multipliers approach where we use partial differential equations for chains propagators q_α in their weak formulations (see appendix A) as constraints. That is, we introduce a Lagrangian \mathcal{L} as

$$\begin{aligned} \mathcal{L} = & \frac{HV}{n} + \sum_{\alpha=1}^M \left[\int_{\Omega} \int_0^{l_\alpha} \left(-q_\alpha \partial_s \hat{\lambda}_\alpha + \mu_\alpha(s) q_\alpha \hat{\lambda}_\alpha + \nabla q_\alpha \cdot \nabla \hat{\lambda}_\alpha \right) ds d\mathbf{r} \right. \\ & \left. + \int_{\Omega} \left(q_\alpha(l_\alpha) \hat{\lambda}_\alpha(l_\alpha) - \hat{\lambda}_\alpha(0) \right) d\mathbf{r} + \sum_{\nu=a,p,w} \int_{\Gamma_\nu} \int_0^{l_\alpha} \eta(\gamma_{\nu,\alpha}(s) - \gamma_{\nu,c}) q_\alpha \hat{\lambda}_\alpha ds d\mathbf{r} \right], \end{aligned}$$

where $\hat{\lambda}_\alpha$ are Lagrangian multipliers associated with the PDE-constraints for q_α . The full derivative of H with respect to τ is then equal to the partial derivative of \mathcal{L} , that is, $\frac{dH}{d\tau} = \frac{\partial \mathcal{L}}{\partial \tau}$, provided that the following optimality conditions are satisfied:

$$\begin{aligned} \delta_{\hat{\lambda}_\alpha} \mathcal{L} &= \int \frac{\delta \mathcal{L}}{\delta \hat{\lambda}_\alpha} \delta \hat{\lambda}_\alpha = 0, \quad \forall \hat{\lambda}_\alpha, \\ \delta_{q_\alpha} \mathcal{L} &= \int \frac{\delta \mathcal{L}}{\delta q_\alpha} \delta q_\alpha = 0, \quad \forall q_\alpha. \end{aligned}$$

It is trivial to show that the first condition recovers the weak form of (14). The second condition provides equations for Lagrangian multipliers $\hat{\lambda}_\alpha$. After explicitly taking the variation of \mathcal{L} with respect to q_α , one obtains the following expression:

$$\begin{aligned}
\delta_{q_\alpha} \mathcal{L} = & \int_{\Omega} \int_0^{l_\alpha} \left(-\delta q_\alpha \partial_s \hat{\lambda}_\alpha + \mu_\alpha(s) \delta q_\alpha \hat{\lambda}_\alpha + \nabla \delta q_\alpha \cdot \nabla \hat{\lambda}_\alpha \right) ds d\mathbf{r} \\
& + \int_{\Omega} \left(\hat{\lambda}_\alpha(l_\alpha) - \frac{\varphi_\alpha(1-G_\alpha)}{Q_\alpha} \right) \delta q_\alpha(l_\alpha) d\mathbf{r} - V \varphi_\alpha G_\alpha \int_{\Gamma_p} g_\alpha(\mathbf{r}) \frac{\delta q_\alpha(l_\alpha)}{q_\alpha(l_\alpha)} d\mathbf{r} \\
& + \sum_{\nu=a,p,w} \int_{\Gamma_\nu} \int_0^{l_\alpha} \eta(\gamma_{\nu,\alpha}(s) - \gamma_{\nu,c}) \delta q_f \hat{\lambda}_f ds d\mathbf{r}
\end{aligned}$$

Using the integration by parts formula (27) leads to which are weak formulations of the following diffusion equations:

$$\begin{aligned}
\delta_{q_\alpha} \mathcal{L} = & \int_{\Omega} \int_0^{l_\alpha} \left(-\delta q_\alpha \partial_s \hat{\lambda}_\alpha + \mu_\alpha(s) \delta q_\alpha \hat{\lambda}_\alpha - \nabla^2 \hat{\lambda}_\alpha \right) \delta q_\alpha ds d\mathbf{r} \\
& + \int_{\Omega} \left(\hat{\lambda}_\alpha(l_\alpha) - \frac{\varphi_\alpha(1-G_\alpha)}{Q_\alpha} \right) \delta q_\alpha(l_\alpha) d\mathbf{r} + \sum_{\nu=a,w} \int_{\Gamma_\nu} \int_0^{l_\alpha} \left(\partial_{\mathbf{n}} \hat{\lambda}_\alpha + \eta(\gamma_{\nu,\alpha}(s) - \gamma_{\nu,c}) \hat{\lambda}_\alpha \right) \delta q_\alpha ds d\mathbf{r}. \\
& + \int_{\Gamma_p} \int_0^{l_\alpha} \left(\partial_{\mathbf{n}} \hat{\lambda}_\alpha + \eta(\gamma_{p,\alpha}(s) - \gamma_{p,c}) \hat{\lambda}_\alpha - V G_\alpha \varphi_\alpha g_\alpha(\mathbf{r}) \frac{\delta(s-l_\alpha)}{q_\alpha(l_\alpha)} \right) \delta q_\alpha ds d\mathbf{r}
\end{aligned}$$

As one can see $\delta_{q_\alpha} \mathcal{L} = 0, \forall q_\alpha$, leads to a weak formulation of the diffusion equation for the Lagrange multiplier $\hat{\lambda}_\alpha$ that is completely analogous to the equation for the complimentary chain propagator \hat{q}_α (15) with the exception that the initial and boundary conditions are scaled by φ_α . Thus, we have $\hat{\lambda}_\alpha = \varphi_\alpha \hat{q}_\alpha$.

We now turn our attention to computing the partial derivative of Lagrangian \mathcal{L} with respect to τ . The only terms in \mathcal{L} that are explicit functions of the problem geometry are domains of integration $\Omega = \Omega(\tau)$, $\Gamma_a = \Gamma_a(\tau)$, $\Gamma_p = \Gamma_p(\tau)$, $\Gamma_w = \Gamma_w(\tau)$, surface energies $\gamma_{pA} = \gamma_{pA}(\mathbf{r}, \tau)$, $\gamma_{pB} = \gamma_{pB}(\mathbf{r}, \tau)$, $\gamma_{wA} = \gamma_{wA}(\mathbf{r}, \tau)$, $\gamma_{wB} = \gamma_{wB}(\mathbf{r}, \tau)$ and grafting density $g = g_\alpha(\mathbf{r}, \tau)$. It can be shown (see appendix B) that for integrals of the form:

$$\int_{\Omega(\tau)} a(\mathbf{r}) d\mathbf{r}, \quad \int_{\Gamma_a(\tau)} a(\mathbf{r}) d\mathbf{r}, \quad \int_{\Gamma_p(\tau)} a(\mathbf{r})b(\mathbf{r}, \tau) d\mathbf{r}, \quad \text{and} \quad \int_{\Gamma_w(\tau)} a(\mathbf{r})c(\mathbf{r}, \tau) d\mathbf{r}, \quad (19)$$

where $a(\mathbf{r})$ is a field independent of τ , while $b(\mathbf{r}, \tau)$ and $c(\mathbf{r}, \tau)$ are fields that follow the nanoparticle and the substrate, correspondingly, the following equations hold true:

$$\begin{aligned} \frac{\partial}{\partial \tau} \int_{\Omega} a d\mathbf{r} &= \int_{\Gamma_a} av_n d\mathbf{r} + \int_{\Gamma_p} a(\mathbf{v}_p - \boldsymbol{\omega}_p \times \mathbf{r}) \cdot \mathbf{n} d\Gamma + \int_{\Gamma_w} a(\mathbf{v}_w - \boldsymbol{\omega}_w \times \mathbf{r}) \cdot \mathbf{n} d\Gamma, \\ \frac{\partial}{\partial \tau} \int_{\Gamma_a} a d\mathbf{r} &= \int_{\Gamma_a} v_n(\kappa + \partial_n) a d\mathbf{r} + \int_{\Gamma_a \cap \Gamma_w} a \frac{v_n \cos(\theta_c) + (\mathbf{v}_w - \boldsymbol{\omega}_w \times \mathbf{r}) \cdot \mathbf{n}_w}{\sin(\theta_c)} d\mathbf{r}, \\ \frac{\partial}{\partial \tau} \int_{\Gamma_p} ab d\mathbf{r} &= \int_{\Gamma_p} (\mathbf{v}_p - \boldsymbol{\omega}_p \times \mathbf{r}) \cdot (\mathbf{n}\kappa ab + \mathbf{n}b\partial_n a - a\nabla_{\perp} b) d\mathbf{r}, \\ \frac{\partial}{\partial \tau} \int_{\Gamma_w} ac d\mathbf{r} &= \int_{\Gamma_w} (\mathbf{v}_w - \boldsymbol{\omega}_w \times \mathbf{r}) \cdot (\mathbf{n}\kappa ac + \mathbf{n}c\partial_n a - a\nabla_{\perp} c) d\mathbf{r} \\ &\quad + \int_{\Gamma_a \cap \Gamma_w} ac \frac{v_n + (\mathbf{v}_w - \boldsymbol{\omega}_w \times \mathbf{r}) \cdot \mathbf{n}_w \cos(\theta_c)}{\sin(\theta_c)} d\mathbf{r}, \end{aligned} \quad (20)$$

where κ is the curvature of the polymer-air interface Γ_a , θ_c is the angle between Γ_a and Γ_w at their intersection, and tangential gradient ∇_{\perp} is defined as $\nabla_{\perp} = \nabla - \mathbf{n}\partial_n$. Applying these formulas while differentiating \mathcal{L} with respect to τ , one arrives at (assuming the volume of the system V is constant):

$$\frac{d}{d\tau} \left(\frac{HV}{n} \right) = \frac{\partial}{\partial \tau} \mathcal{L} \quad (21)$$

$$\begin{aligned} &= \int_{\Gamma_a} \sigma v_n d\mathbf{r} + \int_{\Gamma_a \cap \Gamma_w} f_a^c v_n d\mathbf{r} + \mathbf{v}_p \cdot \int_{\Gamma_p} \mathbf{f}_p d\mathbf{r} + \boldsymbol{\omega}_p \cdot \int_{\Gamma_p} \mathbf{f}_p \times \mathbf{r} d\mathbf{r} \\ &\quad + \mathbf{v}_w \cdot \left[\int_{\Gamma_w} \mathbf{f}_w d\mathbf{r} + \int_{\Gamma_a \cap \Gamma_w} f_w^c \mathbf{n}_w d\mathbf{r} \right] + \boldsymbol{\omega}_w \cdot \left[\int_{\Gamma_w} \mathbf{f}_w \times \mathbf{r} d\mathbf{r} + \int_{\Gamma_a \cap \Gamma_w} f_w^c \mathbf{n}_w \times \mathbf{r} d\mathbf{r} \right], \end{aligned} \quad (22)$$

$$(23)$$

where the surface force densities acting on polymer-air, polymer-particle, and polymer-wall

are given by

$$\begin{aligned}
\sigma &= \Pi + \eta (\kappa + \partial_{\mathbf{n}}) \gamma_{a,\text{eff}}, \\
\mathbf{f}_p &= \Pi \mathbf{n}_p + \eta \mathbf{n}_p \left(\kappa \gamma_{p,\text{eff}} + \gamma_{pA} \partial_{\mathbf{n}} \rho_A + \gamma_{pB} \partial_{\mathbf{n}} \rho_B - \sum_{\alpha=1}^M G_\alpha \varphi_\alpha V \eta^{-1} g_\alpha(\mathbf{r}) \frac{\partial_{\mathbf{n}} Q_\alpha^t}{Q_\alpha^t} \right) \\
&\quad - \eta \left(\rho_A \nabla_{\perp} \gamma_{pA} + \rho_B \nabla_{\perp} \gamma_{pB} - \sum_{\alpha=1}^M G_\alpha \varphi_\alpha V \eta^{-1} \nabla_{\perp} g_\alpha(\mathbf{r}) \log(Q_\alpha^t) \right), \\
\mathbf{f}_w &= \Pi \mathbf{n}_w + \eta \mathbf{n}_w (\kappa (\gamma_{w,\text{eff}} - \gamma_{aw}) + \gamma_{wA} \partial_{\mathbf{n}} \rho_A + \gamma_{wB} \partial_{\mathbf{n}} \rho_B) - (\rho_A \nabla_{\perp} \gamma_{wA} + \rho_B \nabla_{\perp} \gamma_{wB}),
\end{aligned}$$

the line force densities acting on polymer-air and polymer-wall surface at the triple junction are given by

$$\begin{aligned}
f_a^c &= \eta \frac{(\gamma_{w,\text{eff}} - \gamma_{aw}) + \gamma_{a,\text{eff}} \cos \theta_c}{\sin \theta_c}, \\
f_w^c &= \eta \frac{\gamma_{a,\text{eff}} + (\gamma_{w,\text{eff}} - \gamma_{aw}) \cos \theta_c}{\sin \theta_c},
\end{aligned}$$

and where

$$\begin{aligned}
\Pi &= \frac{\mu_-^2}{\chi_{AB} N} - \mu_+ - \sum_{\alpha=1}^M \varphi_\alpha \frac{1}{2} \left[\frac{1 - G_\alpha}{Q_\alpha^f} q_\alpha(l_\alpha) + \hat{q}_\alpha(0) \right], \\
\gamma_{a,\text{eff}} &= \gamma_{aA} \rho_A + \gamma_{aB} \rho_B, \\
\gamma_{w,\text{eff}} &= \gamma_{wA} \rho_A + \gamma_{wB} \rho_B, \\
\gamma_{p,\text{eff}} &= \gamma_{pA} \rho_A + \gamma_{pB} \rho_B - \sum_{\alpha=1}^M G_\alpha \varphi_\alpha V \eta^{-1} g_\alpha(\mathbf{r}) \log(Q_\alpha^t).
\end{aligned}$$

The system is in an equilibrium state when forces and moments acting on the nanoparticle and the substrate are zero:

$$\begin{aligned}
\mathbf{F}_p &= \int_{\Gamma_p} \mathbf{f}_p d\mathbf{r} = 0, & \mathbf{M}_p &= \int_{\Gamma_p} \mathbf{f}_p \times \mathbf{r} d\mathbf{r} = 0, \\
\mathbf{F}_w &= \left[\int_{\Gamma_w} \mathbf{f}_w d\mathbf{r} + \int_{\Gamma_a \cap \Gamma_w} f_w^c \mathbf{n}_w d\mathbf{r} \right] = 0, & \mathbf{M}_w &= \left[\int_{\Gamma_w} \mathbf{f}_w \times \mathbf{r} d\mathbf{r} + \int_{\Gamma_a \cap \Gamma_w} f_w^c \mathbf{n}_w \times \mathbf{r} d\mathbf{r} \right] = 0,
\end{aligned}$$

the normal force density acting on the polymer-air interface is uniform:

$$\sigma - \frac{1}{V} \int_{\Gamma} \sigma d\Gamma = 0$$

and the contact angle at the triple junction satisfies the Young's equation

$$\gamma_w^{\text{eff}} - \gamma_{aw} + \gamma_a^{\text{eff}} \cos(\theta_c) = 0.$$

Numerically, such an equilibrium state can be achieved iteratively by starting from a non-equilibrium configuration and evolving the system's geometry in the direction of energy descent according to:

$$v_{\mathbf{n}} = - \left(\sigma - \frac{1}{V} \int_{\Gamma} \sigma d\Gamma \right), \quad \mathbf{v}_p = -\mathbf{F}_p, \quad \boldsymbol{\omega}_p = -\mathbf{M}_p, \quad \mathbf{v}_w = -\mathbf{F}_w, \quad \boldsymbol{\omega}_w = -\mathbf{M}_w,$$

while imposing the contact angle:

$$\theta_c = \cos^{-1} \left(\frac{\gamma_{aw} - \gamma_w^{\text{eff}}}{\gamma_w^{\text{eff}}} \right).$$

and an appropriate care for preserving the volume of polymer material. In such a way, the energy of the system is forced to decrease until it reaches a local minimum.

4 Numerical aspects

The application of the presented framework for investigating non-trivial situation requires advanced numerical capabilities. Specifically, one needs tools for the description and evolution of irregular interfaces as well as capabilities to solve modified diffusion equations (14) and (15) subject to Robin boundary conditions on such irregular interfaces. In this work, we use a combination of the Level-Set Method, adaptive Cartesian grids and sharp-interface finite-volume methods for solving PDE along the lines of Ouaknin *et al.*,¹³ with the exception that the diffusion equations are solved with a more accurate schemes presented in Bochkov and Gibou.¹⁸ The evolution of the free surface in the normal direction is performed by the semi-implicit advection scheme¹⁹ as described in Min and Gibou.²⁰ We note, however, that the proposed methodology can also be implemented in other numerical frameworks, for example, an interface-fitted finite element method.

5 Results

In this section, we present a number of numerical examples to validate the proposed framework and demonstrate its capabilities. In all examples we consider AB-type diblock copolymer chains of length N and fraction of A segments f .

5.1 Imposing surface energies

We begin with demonstrating the importance of the consistent approach for imposing surface energies presented in section 2 on the following three examples.

In the first example, we consider a flower-shaped domain defined by the zero-isocontour of the following function:

$$\phi_1(x, y) = \sqrt{x^2 + y^2} - 5(1 + 0.3 \cos(5\theta)),$$

where $\theta = \arctan\left(\frac{x}{y}\right)$ is the polar angle. In this example the surface energies are uniform and equal to $\gamma_A = \frac{1}{2\eta}$ and $\gamma_B = -\frac{1}{2\eta}$, that is, the domain's boundary preferentially attracts the polymer component B .

In the second example, we consider a domain formed by the intersection of a disk of radius $r_2 = 6.5R_g$ and a horizontal stripe of width $w_2 = 8R_g$. The straight segments of the domain's boundary preferentially attract the polymer component B , such that the surface energies there are equal to $\gamma_{As} = \frac{1}{2\eta}$ and $\gamma_{Bs} = -\frac{1}{2\eta}$. The curved segments of the domain's boundary preferentially attract the polymer component A , such that the surface energies there are equal to $\gamma_{Ac} = -\frac{1}{2\eta}$ and $\gamma_{Bc} = \frac{1}{2\eta}$.

Finally, in the third example we consider a circular disk of radius $r_3 = 6.5R_g$ located at $(x_3, y_3) = (0.1R_g, 2.1R_g)$ that is cut by a corrugated horizontal line defined as the zero-isocontour of function:

$$\phi_3(x, y) = -y + 0.01 - 0.25 \cos\left(2\pi \frac{x}{\lambda}\right),$$

where $\lambda = 4\sqrt[6]{\frac{8\chi_{AB}N}{3\pi^4}}$. The circular section of the domain's boundary has uniform surface energies $\gamma_{Ac} = \frac{1}{2\eta}$ and $\gamma_{Bc} = -\frac{1}{2\eta}$ (attraction of the component B), while the bottom segment has nonuniform surface energies given by expressions:

$$\begin{aligned}\gamma_{Ab} &= -2.5 \cos\left(2\pi \frac{x}{\lambda}\right), \\ \gamma_{Bb} &= 2.5 \cos\left(2\pi \frac{x}{\lambda}\right).\end{aligned}$$

As a result, the grooves attract the component B while the hills attract the component A .

In all the examples, the parameters of the polymer material are set to $\chi_{AB}N = 30$, $f = 0.33$. Polymer chains are discretized using $n_s = 60$ beads and the grid resolution is $20/256R_g$. The simulations begin with the field μ_- initialized with random values.

Figures 4 and 5 depict the confining geometries considered and the resulting density fields obtained using the original system of SCFT equations and the modified system in (14)-(15), while figures 6 and 7 demonstrate the resulting pressure fields obtained using

the two approaches. As one can see, the solution of the two systems of equations leads to practically indistinguishable density fields, however, the standard approach leads to a singular behavior of μ_+ near domains boundaries, while the proposed approach results in pressure fields with well-defined values everywhere.

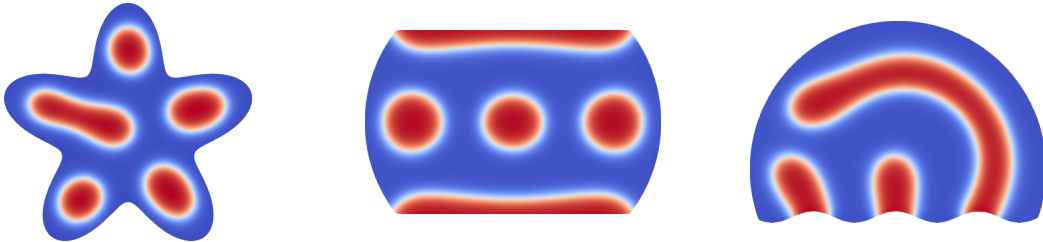


Figure 4: Resulting polymer morphologies obtained using the standard SCFT approach for imposing surface energies.

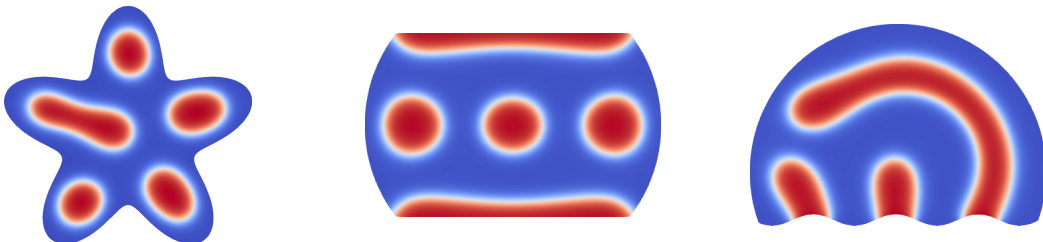


Figure 5: Resulting polymer morphologies obtained using the proposed approach for imposing surface energies.

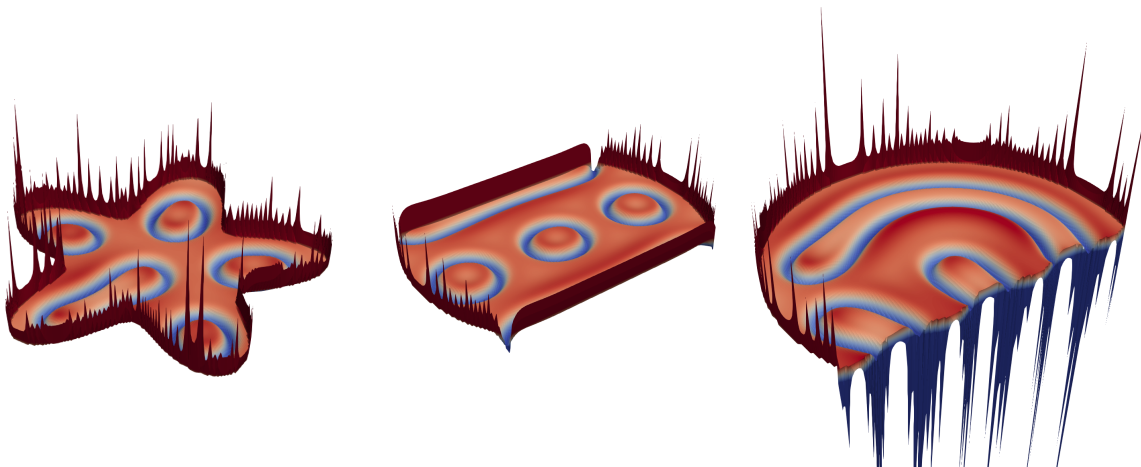


Figure 6: Resulting pressure field μ_+ obtained using the standard SCFT approach for imposing surface energies.

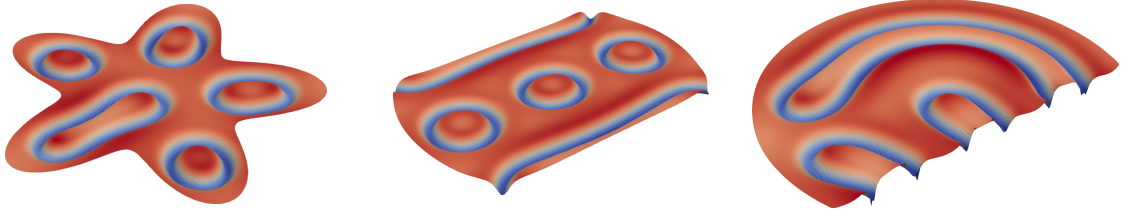


Figure 7: Resulting pressure field μ_+ obtained using the proposed approach for imposing surface energies.

5.2 Validation tests

To validate the obtained expressions for the system energy sensitivity to the free surface shape, we consider a synthetic test in which we externally impose a velocity field for the free surface, we track the change in energy at each iteration and we compare the numerical results to the prediction given in (21). Specifically, we consider a polymer droplet of radius $r = 0.611R_g$ and deform it in the velocity field (v_x, v_y) :

$$\begin{aligned} v_x &= x \cos(5\tau), \\ v_y &= -y \cos(5\tau). \end{aligned} \tag{24}$$

Figure 8 visualize deformations that the polymer droplet undergoes and figure 9 compares

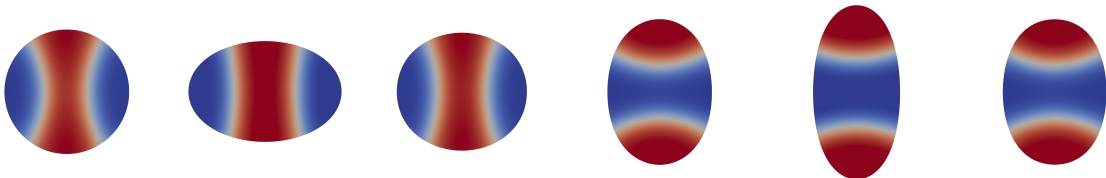


Figure 8: Visualization of imposed deformations in first example from section 5.2.

the predicted and actual changes in energy for each iteration. The predicted values match the actual values very well almost everywhere, except for two spikes that correspond to topology changes in the polymer morphologies where the derived theory does not apply.

Similarly, to validate the energy sensitivity to particles' positions and orientations we consider a synthetic example with imposed velocity. Specifically, we consider three particles – a disk, a rod, and a star – rotating in a circular trajectory and spinning around their center of mass as illustrated in figure 10. Note that the rod has a uniform surface energy, while the

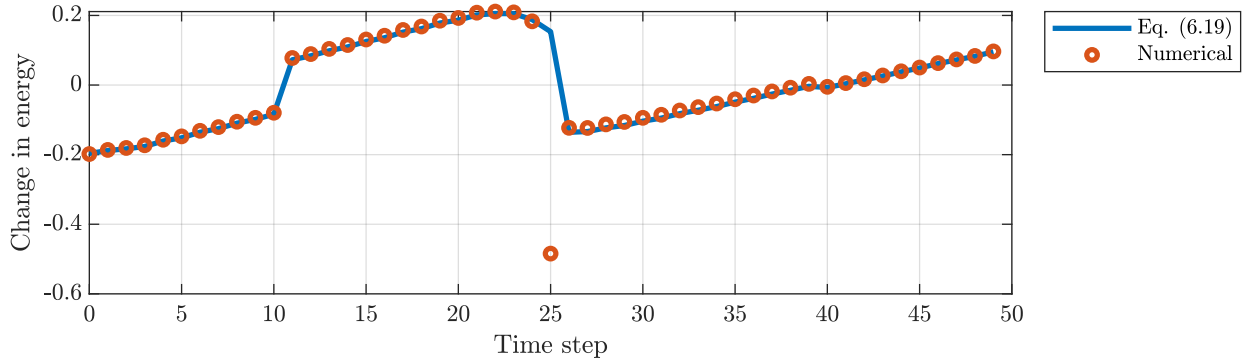


Figure 9: Comparison between changes in energy computed using (21) and numerically for first example in section 5.2.

disk and the star have variable surface energies along their boundaries. Figure 11 compares the predicted and actual values of the energy change for each iteration.

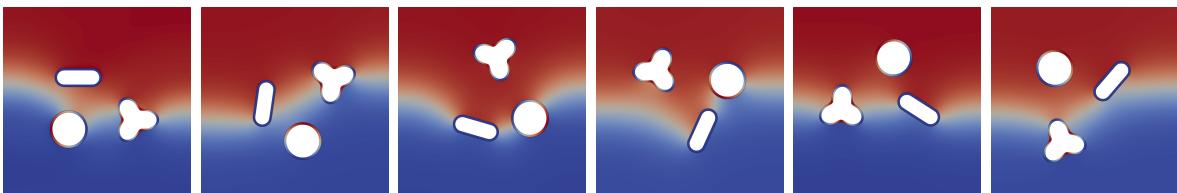


Figure 10: Visualization of imposed motion in second example from section 5.2.

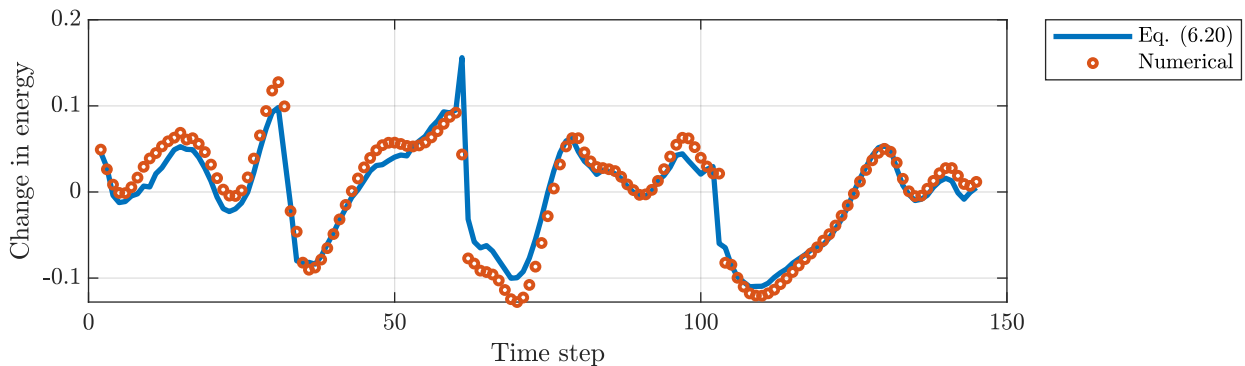


Figure 11: Comparison between changes in energy computed using (21) and numerically for second example in section 5.2.

Again, the predicted values match the numerically computed values well everywhere, except for steps where the topology of polymer morphology undergoes a change. The small deviations between predicted and actual values are attributed to the errors introduced by numerical discretizations.

5.3 Substrate-supported BCP droplets

To demonstrate the capabilities of the proposed framework we consider several representative examples, specifically:

1. A droplet of lamella-forming diblock copolymer ($\chi_{AB}N = 30$, $f = 0.5$) on a substrate with lamellae oriented parallel to the substrate;
2. A droplet of lamella-forming diblock copolymer ($\chi_{AB}N = 30$, $f = 0.5$) on a substrate with lamellae oriented perpendicular to the substrate;
3. A droplet of cylinder-forming diblock copolymer ($\chi_{AB}N = 30$, $f = 0.3$) on a substrate;
4. A droplet of cylinder-forming diblock copolymer ($\chi_{AB}N = 30$, $f = 0.3$) in a groove.

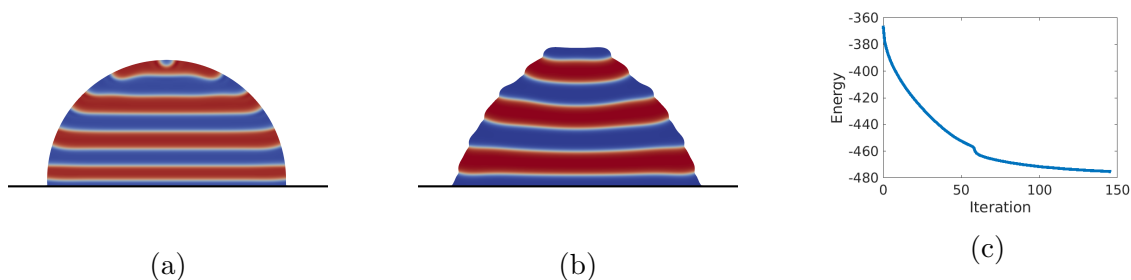


Figure 12: Equilibration of a droplet of a lamella-forming BCP on a substrate with lamellae oriented horizontally: (a) initial state, (b) final state, (c) energy evolution.

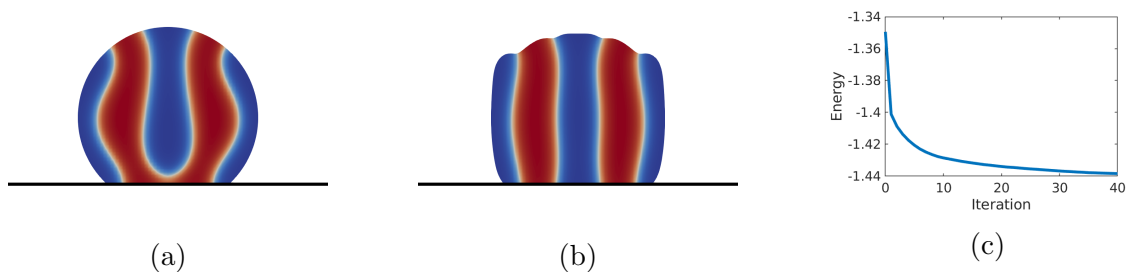


Figure 13: Equilibration of a droplet of a lamella-forming BCP on a substrate with lamellae oriented vertically: (a) initial state, (b) final state, (c) energy evolution.

The simulation results for these cases are presented in figures 14, 12, 13, and 15. Specifically, they demonstrate the initial shape of a polymer droplet, the final shape, and the

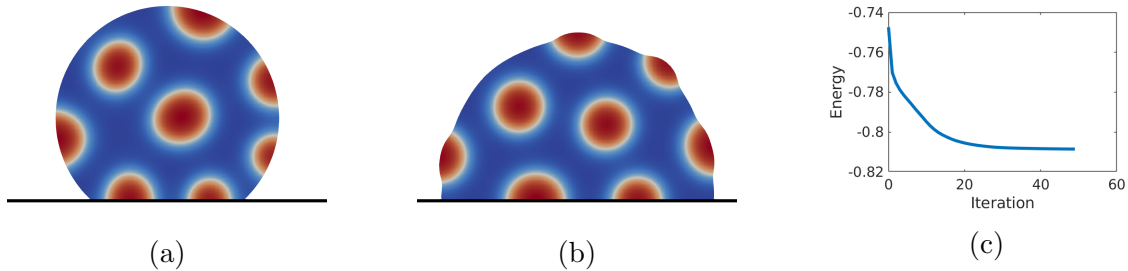


Figure 14: Equilibration of a droplet of a cylinder-forming BCP on a substrate: (a) initial state, (b) final state, (c) energy evolution.

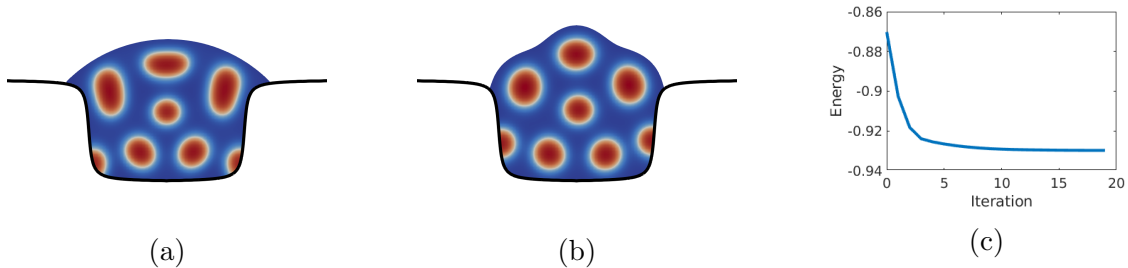


Figure 15: Equilibration of a droplet of a cylinder-forming BCP in a groove: (a) initial state, (b) final state, (c) energy evolution.

energy evolution. As one can see, in all cases the simulated system reaches a local energetic minimum.

5.4 Meniscus formation in graphoepitaxy applications

Next, we apply the presented method to study the meniscus formation in graphoepitaxy applications of block copolymers.^{21,22} Specifically, we consider vertically oriented lamellar-forming and horizontally oriented cylindrical-forming block copolymers in grooves and analyze the influence of the polymer-air surface tension as well as the value of the contact angle on the resulting self-assembling structures of polymer material. The parameters of the problem are chosen in the following way: the width of the groove is $20R_g$, the height of the unperturbed film is $5R_g$, the interaction strength between A and B polymer species is $\chi_{AB}N = 30$, the fraction of the A component is $f = 0.5$ and $f = 0.3$ in the case of lamellae- and cylinder-forming diblock copolymers, respectively. For simplicity, the surface

tensions between the polymer species and the groove's walls are assumed to be equal (i.e., no preferential attraction).

Figures 16 and 17 demonstrate the stable shapes of the polymer films obtained in cases when the contact angle formed by the polymer material with the groove's wall is 60° , 90° , or 120° and for values of polymer-air surface tensions corresponding to $\chi_{ap}N = 1, 9, 25,$ and 100 .

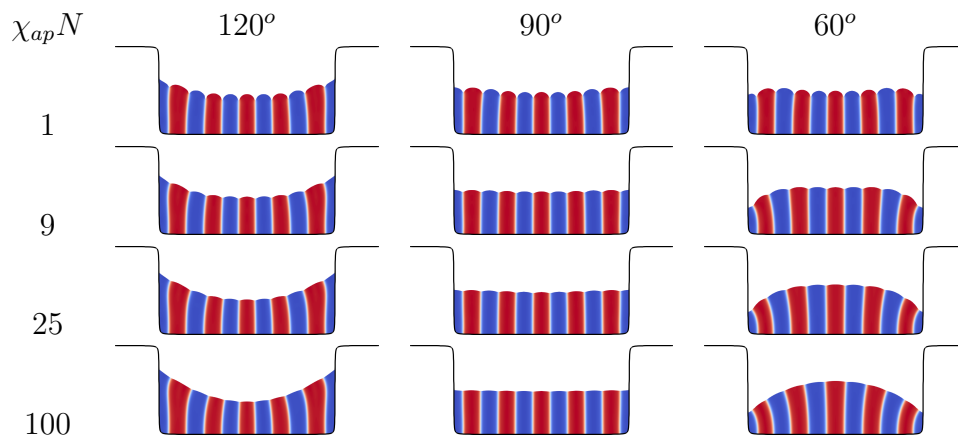


Figure 16: Equilibrium shapes of a lamellae-forming diblock copolymer film of height $4R_g$ in a groove of width $20R_g$ for several values of the polymer-air surface tension and contact angle.

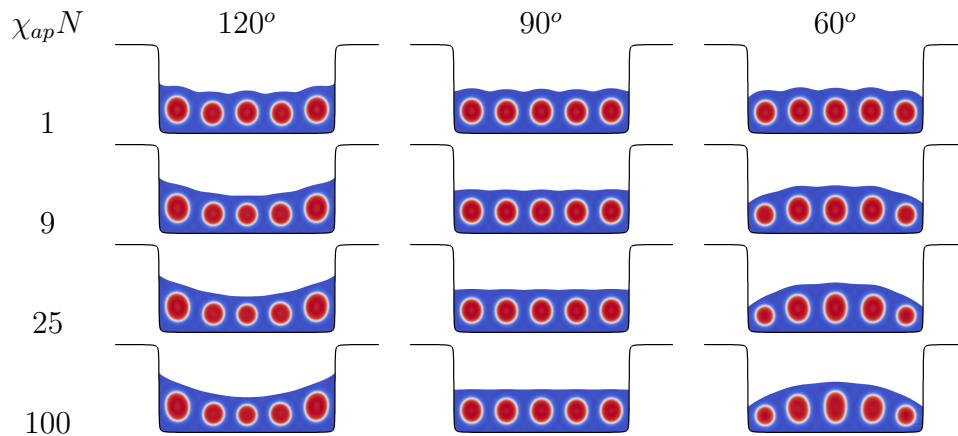


Figure 17: Equilibrium shapes of a cylinder-forming diblock copolymer film of height $4R_g$ in a groove of width $20R_g$ for several values of the polymer-air surface tension and contact angle.

These equilibrium shapes can be qualitatively explained in terms of the balance between

the internal polymer stiffness and the polymer-air surface tension. In cases when the polymer-air surface tension $\chi_{ap}N = 1$ is much lower than the interaction strength between the polymer components $\chi_{AB}N = 30$, the overall film shape remains almost flat with the curvature caused by the meniscus propagating only a very small distance away from the walls. Note that the low surface tension also allows a small-scale corrugation of polymer-air interface due to the internal film morphology. In the other limit when the polymer-air surface tension $\chi_{ap}N = 100$ is much higher than the polymer interaction strength $\chi_{AB}N = 30$, the overall film shapes are very close to the spherical ones expected for simple liquids with only a slight small-scale corrugations. Note that in this case, the polymer domains next to groove's walls also undergo significant deformations. Finally, in intermediate cases $\chi_{ap}N = 9$ and $\chi_{ap}N = 25$, which are comparable to $\chi_{AB}N = 30$, the curvature due to the meniscus formation propagates a significant distance away from the walls, while the center region of the film is still flat.

It is also interesting to see that the degree of the film deformation is slightly higher in the case of lamellae-forming diblock copolymer as demonstrated in figure 18. This indicates that the stiffness of the cylindrical morphology is slightly higher and the deformation of a cylindrical arrangement of polymer chains causes a higher energetic penalty compared to the deformation of the lamellar arrangements.

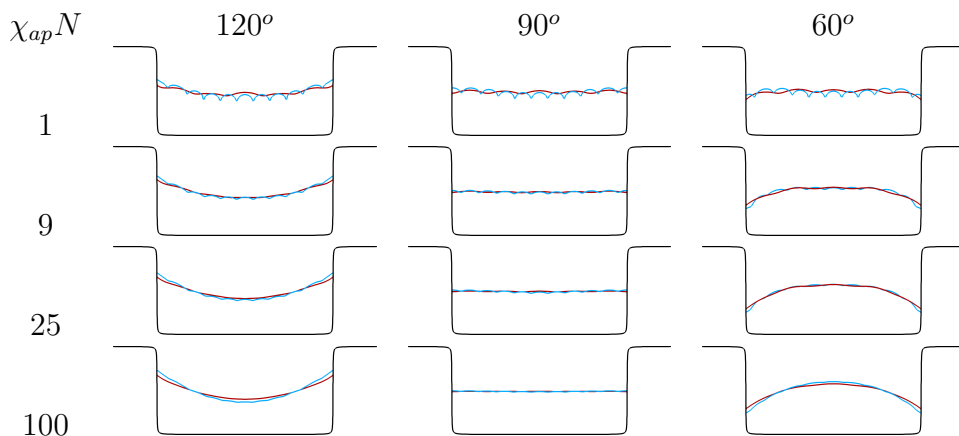


Figure 18: Comparison of the equilibrium shapes of lamellae-forming (blue line) and cylinder-forming (red line) diblock copolymer films of height $4R_g$ in a groove of width $20R_g$ for several values of the polymer-air surface tension and contact angle.

To summarize, the result presented in this example demonstrate that the overall equilibrium shapes of copolymer films in guiding grooves are defined by the balance between the internal stiffness of polymer morphologies and the polymer-air surface tension. These results indicate that in graphoepitaxy applications of block copolymer, the surface energies of guiding templates must be carefully selected to prevent significant deformations of the self-assembling films.

5.5 Placement of Janus rods in lamellae-forming BCP

We now apply the proposed computational approach for investigating the co-assembly of lamellar diblock copolymer ($\chi_{AB}N = 30$, $f = 0.5$) with rod-like Janus particles, that is, particles that are attracted to the A polymer component on the one end and to the the B polymer component on the other end. On the one hand, the elongated shape of such particles promotes the orientation parallel to the AB interface to reduce the system's energy, while the selective attraction on opposite sides of such particles favors the perpendicular orientation. As the result, one can expect the resulting placement of the nanoparticle to be a function of its length and the magnitude of its surface energy. Another factor expected to affect the particle placement is the particles density because the crowding may result in insufficient space for nanoparticles to assume their equilibrium orientation.

In numerical simulations, we consider particles of capsule-like shapes with radius of curvature $r_0 = 0.1R_g$ and nonuniform surface energies given by:

$$\begin{aligned}\gamma_{Ap} &= \frac{1}{\sigma} \frac{1}{2} \sqrt{\chi_{ap}N} (1 + \cos(\theta)), \\ \gamma_{Bp} &= \frac{1}{\sigma} \frac{1}{2} \sqrt{\chi_{ap}N} (1 - \cos(\theta)),\end{aligned}$$

where θ is the angle of rotation from the particle's axis and $\chi_{ap}N$ characterizes the strength of preferential attraction between the nanoparticle and polymer species and, for convenience, is also referred to as *the polarization strength*.

Figure 19 depicts a representative simulation result for the co-assembly of lamellae-forming diblock copolymer ($\chi_{AB}N = 30$, $f = 0.5$) with Janus nanorods of length $0.4R_g$ in a computational domain of dimensions $3R_g \times 3R_g$. One observes that, while a small number of nanoparticles are trapped inside of A or B domains the majority of nanorods tend to aggregate at the interface between A and B polymer components and form a certain angle with the interface. In order to investigate this co-assembly behavior in greater detail, we

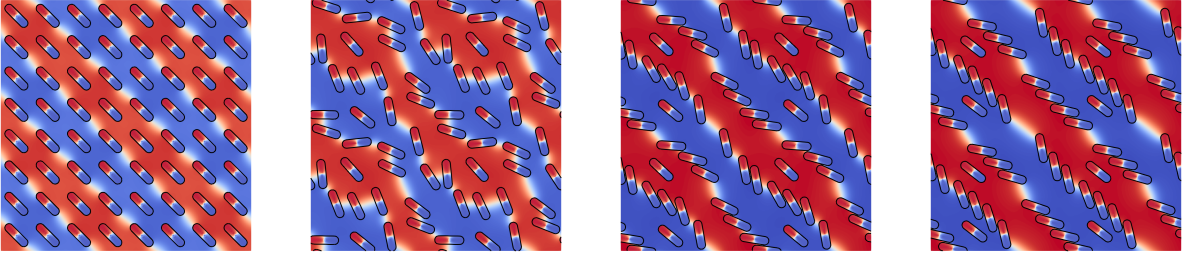


Figure 19: Representative simulation results for co-assembly of a lamellar diblock copolymer ($\chi_{AB}N = 30$, $f = 0.5$) and Janus nanorods of length $0.4R_g$ (periodically tiled for visualization purposes).

first consider a single nanorod in a smaller rectangular domain with dimension $1.8 \times 1.8R_g$, which approximately corresponds to the single diblock lamellar spacing. Periodic boundary conditions are imposed in the x -direction and homogeneous Neumann boundary conditions are imposed in the y -direction. Figure 20 depicts the equilibrium placements of nanorods of different lengths and for several values of the polarization strength $\chi_{ap}N$, while figure 21 summarizes the quantitative values for the equilibrium angles. It is clear from these results that the stable orientation of an isolated Janus nanorod in a lamellar diblock copolymer with respect to the interface between polymer components is a smooth function of the particle's length and of the polarization strength.

Next, we perform similar simulations but this time with different numbers of nanoparticles inside the computational domain. Figures 22 illustrate the obtained particles configurations and figure 23 presents the quantitative results describing these configurations. One can observe that, as long as the density of particles is low (1-3 particles) and no crowding occurs,

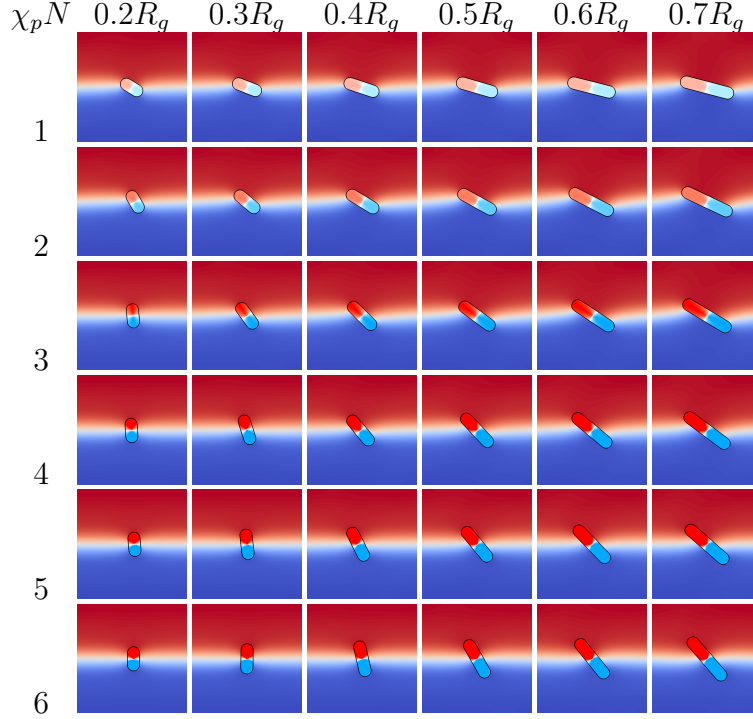


Figure 20: Equilibrium orientation of a Janus nanorod at the interface between A and B blocks obtained for different values of the particle's lengths and of the polarization strength.

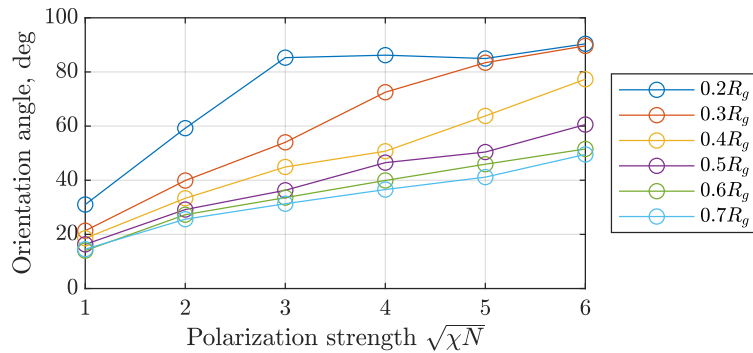


Figure 21: Dependence of the Janus nanorod orientation on the polarization strength for several values of the particle's length.

the equilibrium orientations of nanorods are almost identical to those of a isolated nanorod. As the density of particles is increased, the equilibrium orientations of nanorods dramatically changes due to crowding effects. First, the equilibrium orientation angle increases for each polarization strength value as the particle density increases. Second, as the polarization strength decreases to low values the equilibrium orientation converges to a minimal nonzero value, which is dictated by the geometrical constraint due to crowding, and, thus,

the accessible range of the particles' orientation is reduced.

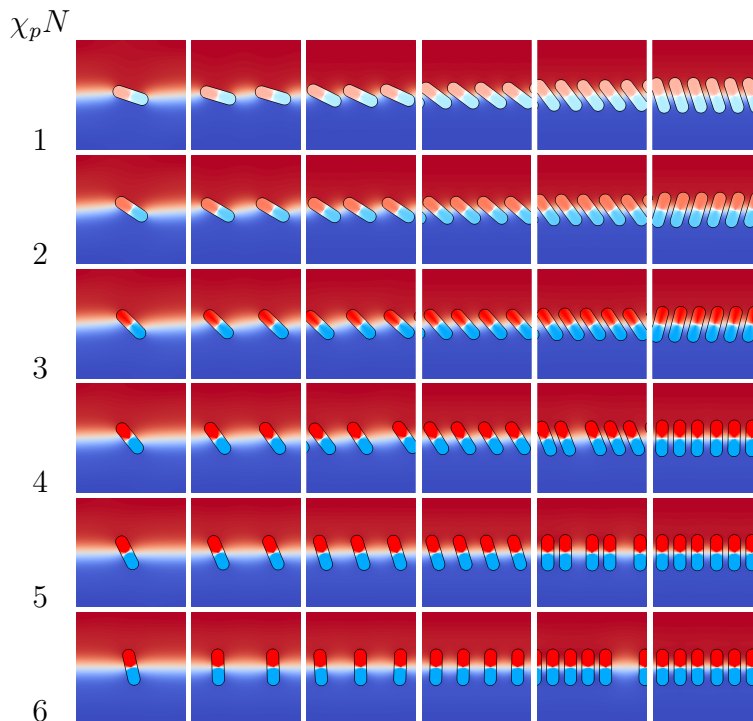


Figure 22: Equilibrium orientation of Janus nanorods at the interface between A and B blocks obtained for different values of the particles density and the polarization strength.

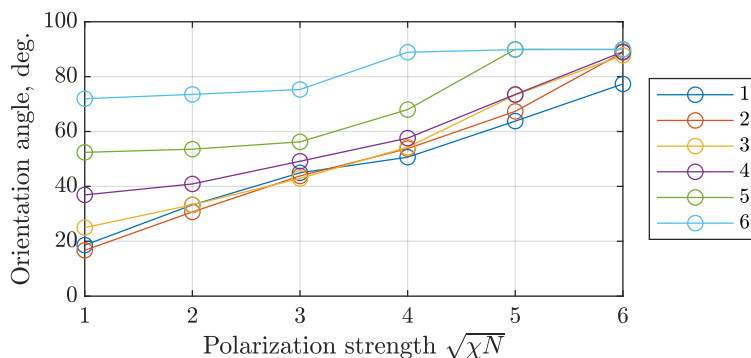


Figure 23: Dependence of the Janus nanorod orientation on the polarization strength for several values of the particles density.

To summarize the findings from numerical simulations of the co-assembly of Janus nanorods in a lamellar-forming diblock copolymer, we observed an aggregation of nanoparticles along interfaces between dissimilar polymer species oriented at a well defined angle with respect to these interfaces. The angle value of the equilibrium orientation continuously depend on the

nanorod’s length and on the polarization strength. High particle densities influence the equilibrium placement of nanorods due to the crowding effect, limiting the minimum achievable angle values.

6 Conclusion

In this work we have presented a generalized theory in the context of Self-Consistent Field Theory that describes equilibrium of polymer free surfaces and submerged nanoparticles. The theory applies to free and tethered polymer chains, substrates and nanoparticles of any shapes, and arbitrary non-uniform surface energies and surface grafting densities. The surface tensions between the polymer material and its surroundings as well as tethered polymer chains are modeled using a consistent unified approach that results in pressure fields free of numerical singularities. The proposed theory has been validated on benchmark examples with imposed velocities and demonstrated a very close match between predicted and actual changes in the system energy.

The proposed theory was applied to the investigation of the meniscus formation in the context of graphoepitaxy applications for lamellar and cylindrical diblock copolymers. It was shown that in case of the lamella-forming copolymer the polymer-air surface tension, as well as the contact angle value at the air-polymer-wall triple junction point affect the distribution of polymer material inside the guiding groove and also cause the bending of polymer lamellar domains. At the same time the cylinder-forming polymer morphology demonstrated less sensitivity to these parameters. In another example, we investigated the placement and orientation of “polarized” nanorod particle in lamellar diblock copolymer. It was demonstrated that such particles aggregate at the interface between dissimilar polymer blocks and that their resulting orientation is controlled by the balance of the particles’ length, the “polarization” strength, and the particles density.

Future research will include the application of the presented methods to cases of grafted

polymers, polymers of more complex architectures, and blends of copolymers. Another direction of future work will be the extension of the presented methods to a more accurate fluctuating field-theoretic description of block copolymers.

Acknowledgement

This research was supported by NSF DMS 1620471.

References

- (1) Matsen, M. W. The standard Gaussian model for block copolymer melts. *Journal of Physics: Condensed Matter* **2001**, *14*, R21.
- (2) Fredrickson, G. H. *The equilibrium theory of inhomogeneous polymers*; Oxford University Press, USA, 2006; Vol. 134.
- (3) Croll, A. B.; Massa, M. V.; Matsen, M. W.; Dalnoki-Veress, K. Droplet shape of an anisotropic liquid. *Physical Review Letters* **2006**, *97*, 204502.
- (4) Maher, M. J.; Self, J. L.; Stasiak, P.; Blachut, G.; Ellison, C. J.; Matsen, M. W.; Bates, C. M.; Willson, C. G. Structure, Stability, and Reorganization of 0.5 L 0 Topography in Block Copolymer Thin Films. *ACS nano* **2016**, *10*, 10152–10160.
- (5) Kim, J. U.; Matsen, M. W. Droplets of structured fluid on a flat substrate. *Soft Matter* **2009**, *5*, 2889–2895.
- (6) Stasiak, P.; McGraw, J. D.; Dalnoki-Veress, K.; Matsen, M. W. Step edges in thin films of lamellar-forming diblock copolymer. *Macromolecules* **2012**, *45*, 9531–9538.
- (7) Carpenter, C. L.; Delaney, K. T.; Laachi, N.; Fredrickson, G. H. Directed self-assembly of diblock copolymers in cylindrical confinement: effect of underfilling and air-polymer

- interactions on configurations. *SPIE Advanced Lithography* **2015**, *9423*, 94231Z, DOI: 10.1117/12.2085639.
- (8) Ouaknin, G.; Laachi, N.; Bochkov, D.; Delaney, K.; Fredrickson, G. H.; Gibou, F. Functional level-set derivative for a polymer self consistent field theory Hamiltonian. *J. Comput. Phys.* **2017**, *345*, 207–223.
- (9) Bockstaller, M. R.; Mickiewicz, R. A.; Thomas, E. L. Block copolymer nanocomposites: perspectives for tailored functional materials. *Advanced materials* **2005**, *17*, 1331–1349.
- (10) Sides, S. W.; Kim, B. J.; Kramer, E. J.; Fredrickson, G. H. Hybrid particle-field simulations of polymer nanocomposites. *Physical review letters* **2006**, *96*, 250601.
- (11) Thompson, R. B.; Ginzburg, V. V.; Matsen, M. W.; Balazs, A. C. Predicting the mesophases of copolymer-nanoparticle composites. *Science* **2001**, *292*, 2469–2472.
- (12) Koski, J.; Chao, H.; Riggleman, R. A. Field theoretic simulations of polymer nanocomposites. *The Journal of chemical physics* **2013**, *139*, 244911.
- (13) Ouaknin, G.; Laachi, N.; Delaney, K.; Fredrickson, G. H.; Gibou, F. Self-consistent field theory simulations of polymers on arbitrary domains. *J. Comput. Phys.* **2016**, *327*, 168 – 185, DOI: <http://dx.doi.org/10.1016/j.jcp.2016.09.021>.
- (14) Müller, M. Phase diagram of a mixed polymer brush. *Physical Review E* **2002**, *65*, 030802.
- (15) Matsen, M. Thin films of block copolymer. *The Journal of chemical physics* **1997**, *106*, 7781–7791.
- (16) Matsen, M. W.; Griffiths, G. H. Melt brushes of diblock copolymer. *The European Physical Journal E* **2009**, *29*, 219–227.

- (17) Chantawansri, T. L.; Hur, S.-M.; García-Cervera, C. J.; Cenicerros, H. D.; Fredrickson, G. H. Spectral collocation methods for polymer brushes. *The Journal of chemical physics* **2011**, *134*, 244905.
- (18) Bochkov, D.; Gibou, F. Solving Poisson-type equations with Robin boundary conditions on piecewise smooth interfaces. *J. Comput. Phys.* **2019**, *376*, 1156–1198.
- (19) Smereka, P. Semi-Implicit Level Set Methods for Curvature and Surface Diffusion Motion. *Journal of Scientific Computing* **2003**, *19*.
- (20) Min, C.; Gibou, F. A second order accurate level set method on non-graded adaptive Cartesian grids. *J. Comput. Phys.* **2007**, *225*, 300–321.
- (21) Jeong, S.-J.; Kim, J. E.; Moon, H.-S.; Kim, B. H.; Kim, S. M.; Kim, J. B.; Kim, S. O. Soft graphoepitaxy of block copolymer assembly with disposable photoresist confinement. *Nano letters* **2009**, *9*, 2300–2305.
- (22) Jeong, S.-J.; Kim, J. Y.; Kim, B. H.; Moon, H.-S.; Kim, S. O. Directed self-assembly of block copolymers for next generation nanolithography. *Materials today* **2013**, *16*, 468–476.
- (23) Sethian, J. A. *Level set methods and fast marching methods*; Cambridge University Press, 1998.
- (24) Osher, S.; Fedkiw, R. P. *Level set methods and dynamic implicit surfaces*; Springer, 2003; Vol. 153.
- (25) Zhao, H.-K.; Chan, T.; Merriman, B.; Osher, S. A variational level set approach to multiphase motion. *Journal of computational physics* **1996**, *127*, 179–195.

A Weak formulations and equivalence of modified diffusion equations

To demonstrate the equivalence of (2) and (9) we invoke their weak forms. Multiplying the diffusion equation in (2) by an test function $\psi(s, \mathbf{r})$ and integrating over domain Ω and contour variable range $s \in [0, 1]$ we obtain:

$$\int_{\Omega} \int_0^1 (\partial_s q + (\mu(s) + \eta\gamma(s)\delta_{\Gamma}) q - \nabla^2 q) \psi \, d\mathbf{r} \, ds = 0. \quad (25)$$

Using integration by parts and the divergence theorem it is straightforward to show that:

$$\begin{aligned} \int_{\Omega} \int_0^1 \partial_s q \psi \, d\mathbf{r} \, ds &= \int_{\Omega} \partial_s (q\psi) \, d\mathbf{r} \, ds - \int_{\Omega} \int_0^1 q \partial_s \psi \, d\mathbf{r} \, ds \\ &= \int_{\Omega} (q(1, \mathbf{r})\psi(1, \mathbf{r}) - q(0, \mathbf{r})\psi(0, \mathbf{r})) \, d\mathbf{r} \, ds - \int_{\Omega} \int_0^1 q \partial_s \psi \, d\mathbf{r} \, ds \end{aligned} \quad (26)$$

and

$$\begin{aligned} \int_{\Omega} \int_0^1 \nabla^2 q \psi \, d\mathbf{r} \, ds &= \int_{\Omega} \int_0^1 \nabla \cdot (\nabla q \psi) \, d\mathbf{r} \, ds - \int_{\Omega} \int_0^1 \nabla q \cdot \nabla \psi \, d\mathbf{r} \, ds \\ &= \int_{\Gamma} \int_0^1 \partial_n q \psi \, d\mathbf{r} \, ds - \int_{\Omega} \int_0^1 \nabla q \cdot \nabla \psi \, d\mathbf{r} \, ds. \end{aligned} \quad (27)$$

Using the above two expressions in (25) along with the initial and boundary conditions for q produces the following weak form of (2):

$$\int_{\Omega} (q(1, \mathbf{r})\psi(1, \mathbf{r}) - \psi(0, \mathbf{r})) d\mathbf{r} ds + \int_{\Omega} \int_0^1 (-q\partial_s\psi + (\mu(s) + \eta\gamma(s)\delta_{\Gamma})q\psi + \nabla q \cdot \nabla\psi) d\mathbf{r} ds = 0, \quad \forall\psi$$

Converting the term containing surface delta function δ_{Γ} into a boundary integral as

$$\int_{\Omega} \int_0^1 \eta\gamma(s)\delta_{\Gamma}q\psi d\mathbf{r} ds = \int_{\Gamma} \int_0^1 \eta\gamma(s)q\psi d\mathbf{r} ds$$

the obtained weak form can be transformed into

$$\int_{\Omega} (q(1, \mathbf{r})\psi(1, \mathbf{r}) - \psi(0, \mathbf{r})) d\mathbf{r} ds + \int_{\Omega} \int_0^1 (-q\partial_s\psi + \mu(s)q\psi + \nabla q \cdot \nabla\psi) d\mathbf{r} ds + \int_{\Gamma} \int_0^1 \eta\gamma(s)q\psi d\mathbf{r} ds = 0, \quad \forall\psi,$$

which represents a weak form an altered diffusion equation. Indeed, using formulas (26) and (27) in the reverse way, one can write the above expression as

$$\int_{\Omega} (q(0, \mathbf{r}) - 1) \psi(0, \mathbf{r}) d\mathbf{r} ds + \int_{\Omega} \int_0^1 (\partial_s q + \mu(s)q - \nabla^2 q) \psi d\mathbf{r} ds + \int_{\Gamma} \int_0^1 (\partial_n q + \eta\gamma(s)q) \psi d\mathbf{r} ds = 0, \quad \forall\psi$$

from which it immediately follows that q satisfies (9). The equivalence of (5)-(10), (9)-(12), and (10)-(13) can be demonstrated in the analogous fashion.

B Shape derivatives of integral quantities

In order to calculate derivatives of integral quantities (19) we employ the Level-Set methodology.^{23,24} Specifically, we represent domain $\Omega(\tau)$ as the intersection of three smooth domains

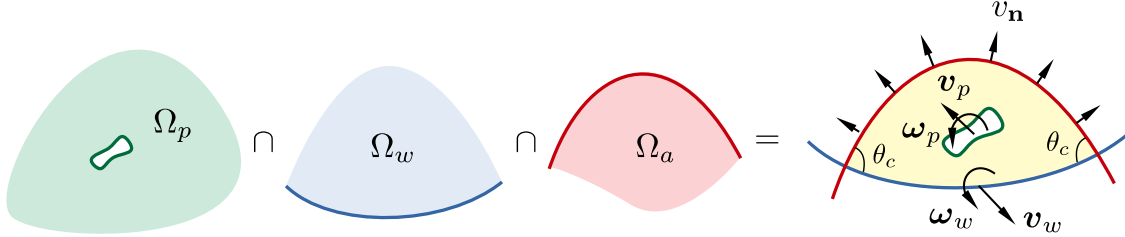


Figure 24: Problem geometry and notation used in section B.

$\Omega_a(\tau)$, $\Omega_p(\tau)$, and Ω_w as demonstrated in figure 24, and, second, that boundaries of domains $\Omega_a(\tau)$, $\Omega_p(\tau)$, and Ω_w are described as zero-isocontours of higher-dimensional functions $\phi_a(\tau)$, $\phi_p(\tau)$, and ϕ_w , called *level-set functions*, such that:

$$\phi_a(\tau) \begin{cases} < 0, & \mathbf{r} \in \Omega_a(\tau), \\ > 0, & \mathbf{r} \notin \Omega_a(\tau), \end{cases} \quad \phi_p(\tau) \begin{cases} < 0, & \mathbf{r} \in \Omega_p(\tau), \\ > 0, & \mathbf{r} \notin \Omega_p(\tau), \end{cases} \quad \text{and} \quad \phi_w \begin{cases} < 0, & \mathbf{r} \in \Omega_w, \\ > 0, & \mathbf{r} \notin \Omega_w. \end{cases}$$

In this setting the evolution of domain $\Omega_a(\tau)$ in the velocity field $v_n(\tau)$ and the motion of domain $\Omega_p(\tau)$ with translational and rotational velocities \mathbf{v}_p and $\boldsymbol{\omega}_p$ are described by advection equations for function $\phi_a(\tau)$ and $\phi_p(\tau)$ as

$$\frac{\partial \phi_a}{\partial \tau} + v_n |\nabla \phi_a| = 0, \quad (28)$$

$$\frac{\partial \phi_p}{\partial \tau} + (\mathbf{v}_p - \mathbf{r} \times \boldsymbol{\omega}_p) \cdot \mathbf{n} |\nabla \phi_p| = 0, \quad (29)$$

$$\frac{\partial \phi_w}{\partial \tau} + (\mathbf{v}_w - \mathbf{r} \times \boldsymbol{\omega}_w) \cdot \mathbf{n} |\nabla \phi_w| = 0. \quad (30)$$

The evolution of a field $b(\tau)$ that moves along with domain $\Omega_p(\tau)$ is described by a similar equation:

$$\frac{\partial b}{\partial \tau} + (\mathbf{v}_p - \mathbf{r} \times \boldsymbol{\omega}_p) \cdot \nabla b = 0, \quad (31)$$

$$\frac{\partial c}{\partial \tau} + (\mathbf{v}_w - \mathbf{r} \times \boldsymbol{\omega}_w) \cdot \nabla c = 0. \quad (32)$$

The description of the problem geometry in this way allows to write the boundary and domain integrals using the Heaviside step functions $H(x)$, Dirac delta distribution $\delta(x)$ and the co-area formula as

$$\begin{aligned} \int_{\Omega} a \, d\mathbf{r} &= \int_{\mathcal{R}^D} a H(-\phi_a) H(-\phi_p) H(-\phi_w) \, d\mathbf{r}, \\ \int_{\Gamma_a} a \, d\mathbf{r} &= \int_{\mathcal{R}^D} a \delta(\phi_a) |\nabla \phi_a| H(-\phi_p) H(-\phi_w) \, d\mathbf{r}, \\ \int_{\Gamma_p} ab(\tau) \, d\mathbf{r} &= \int_{\mathcal{R}^D} ab(\tau) H(-\phi_a) \delta(\phi_p) |\nabla \phi_p| H(-\phi_w) \, d\mathbf{r}, \\ \int_{\Gamma_w} ac(\tau) \, d\mathbf{r} &= \int_{\mathcal{R}^D} ac(\tau) H(-\phi_a) H(-\phi_p) \delta(\phi_w) |\nabla \phi_w| \, d\mathbf{r}, \end{aligned}$$

where \mathcal{D} denotes the problem's dimensionality. Taking the derivative of these expression with respect to τ leads to

$$\begin{aligned}
\frac{\partial}{\partial \tau} \int_{\Omega} a \, d\mathbf{r} &= - \int_{\mathcal{R}^{\mathcal{D}}} a \delta(-\phi_a) \frac{\partial \phi_a}{\partial \tau} H(-\phi_p) H(-\phi_w) \, d\mathbf{r} - \int_{\mathcal{R}^{\mathcal{D}}} a H(-\phi_a) \delta(-\phi_p) \frac{\partial \phi_p}{\partial \tau} H(-\phi_w) \, d\mathbf{r} \\
&\quad - \int_{\mathcal{R}^{\mathcal{D}}} a H(-\phi_a) H(-\phi_p) \delta(-\phi_w) \frac{\partial \phi_w}{\partial \tau} \, d\mathbf{r}, \\
\frac{\partial}{\partial \tau} \int_{\Gamma_a} a \, d\mathbf{r} &= \int_{\mathcal{R}^{\mathcal{D}}} a \delta'(\phi_a) \frac{\partial \phi_a}{\partial \tau} |\nabla \phi_a| H(-\phi_p) H(-\phi_w) \, d\mathbf{r} + \int_{\mathcal{R}^{\mathcal{D}}} a \delta(\phi_a) \frac{\nabla \phi_a}{|\nabla \phi_a|} \cdot \nabla \frac{\partial \phi_a}{\partial \tau} H(-\phi_p) H(-\phi_w) \, d\mathbf{r} \\
&\quad - \int_{\mathcal{R}^{\mathcal{D}}} a \delta(\phi_a) |\nabla \phi_a| \delta(-\phi_p) \frac{\partial \phi_p}{\partial \tau} H(-\phi_w) \, d\mathbf{r} - \int_{\mathcal{R}^{\mathcal{D}}} a \delta(\phi_a) |\nabla \phi_a| H(-\phi_p) \delta(-\phi_w) \frac{\partial \phi_w}{\partial \tau} \, d\mathbf{r}, \\
\frac{\partial}{\partial \tau} \int_{\Gamma_p} ab(\tau) \, d\mathbf{r} &= \int_{\mathcal{R}^{\mathcal{D}}} a \frac{\partial b}{\partial \tau} H(-\phi_a) \delta(\phi_p) |\nabla \phi_p| H(-\phi_w) \, d\mathbf{r} - \int_{\mathcal{R}^{\mathcal{D}}} ab \delta(-\phi_a) \frac{\partial \phi_a}{\partial \tau} \delta(\phi_p) |\nabla \phi_p| H(-\phi_w) \, d\mathbf{r} \\
&\quad + \int_{\mathcal{R}^{\mathcal{D}}} ab H(-\phi_a) \delta'(\phi_p) \frac{\partial \phi_p}{\partial \tau} |\nabla \phi_p| H(-\phi_w) \, d\mathbf{r} + \int_{\mathcal{R}^{\mathcal{D}}} ab H(-\phi_a) \delta(\phi_p) \frac{\nabla \phi_p}{|\nabla \phi_p|} \cdot \nabla \frac{\partial \phi_p}{\partial \tau} H(-\phi_w) \, d\mathbf{r}, \\
&\quad - \int_{\mathcal{R}^{\mathcal{D}}} ab H(-\phi_a) \delta(\phi_p) |\nabla \phi_p| \delta(-\phi_w) \frac{\partial \phi_w}{\partial \tau} \, d\mathbf{r} \\
\frac{\partial}{\partial \tau} \int_{\Gamma_w} ac(\tau) \, d\mathbf{r} &= \int_{\mathcal{R}^{\mathcal{D}}} a \frac{\partial c}{\partial \tau} H(-\phi_a) \delta(\phi_w) |\nabla \phi_w| H(-\phi_p) \, d\mathbf{r} - \int_{\mathcal{R}^{\mathcal{D}}} ac \delta(-\phi_a) \frac{\partial \phi_a}{\partial \tau} H(-\phi_p) \delta(\phi_w) |\nabla \phi_w| \, d\mathbf{r} \\
&\quad + \int_{\mathcal{R}^{\mathcal{D}}} ac H(-\phi_a) H(-\phi_p) \delta'(\phi_w) \frac{\partial \phi_w}{\partial \tau} |\nabla \phi_w| \, d\mathbf{r} + \int_{\mathcal{R}^{\mathcal{D}}} ac H(-\phi_a) H(-\phi_p) \delta(\phi_w) \frac{\nabla \phi_w}{|\nabla \phi_w|} \cdot \nabla \frac{\partial \phi_w}{\partial \tau} \, d\mathbf{r}, \\
&\quad - \int_{\mathcal{R}^{\mathcal{D}}} ac H(-\phi_a) \delta(-\phi_p) \frac{\partial \phi_p}{\partial \tau} \delta(\phi_w) |\nabla \phi_w| \, d\mathbf{r}, \quad (33)
\end{aligned}$$

Using the integration by parts²⁵ the terms containing gradients of temporal derivatives can be transformed as

$$\begin{aligned}
\int_{\mathcal{R}^D} a\delta(\phi_a)\frac{\nabla\phi_a}{|\nabla\phi_a|}\cdot\nabla\frac{\partial\phi_a}{\partial\tau}H(-\phi_p)H(-\phi_w) d\mathbf{r} &= -\int_{\mathcal{R}^D}\frac{\partial\phi_a}{\partial\tau}\nabla\cdot\left(a\delta(\phi_a)\frac{\nabla\phi_a}{|\nabla\phi_a|}H(-\phi_p)H(-\phi_w)\right) d\mathbf{r} \\
&= -\int_{\mathcal{R}^D}\frac{\partial\phi_a}{\partial\tau}\left(\delta(\phi_a)H(-\phi_p)H(-\phi_w)\left(\nabla\cdot\frac{\nabla\phi_a}{|\nabla\phi_a|}+\frac{\nabla\phi_a}{|\nabla\phi_a|}\cdot\nabla\right)a\right. \\
&\quad \left.+a\delta'(\phi_a)|\nabla\phi_a|H(-\phi_p)H(-\phi_w)\right. \\
&\quad \left.-a\delta(\phi_a)\delta(-\phi_p)\nabla\phi_p\cdot\frac{\nabla\phi_a}{|\nabla\phi_a|}H(-\phi_w)-a\delta(\phi_a)H(-\phi_p)\delta(-\phi_w)\nabla\phi_w\cdot\frac{\nabla\phi_a}{|\nabla\phi_a|}\right) d\mathbf{r} \\
&= -\int_{\mathcal{R}^D}\frac{\partial\phi_a}{\partial\tau}\left(\delta(\phi_a)H(-\phi_p)H(-\phi_w)\left(\nabla\cdot\frac{\nabla\phi_a}{|\nabla\phi_a|}+\frac{\nabla\phi_a}{|\nabla\phi_a|}\cdot\nabla\right)a\right. \\
&\quad \left.+a\delta'(\phi_a)|\nabla\phi_a|H(-\phi_p)H(-\phi_w)-a\delta(\phi_a)H(-\phi_p)\delta(-\phi_w)\nabla\phi_w\cdot\frac{\nabla\phi_a}{|\nabla\phi_a|}\right) d\mathbf{r}.
\end{aligned}$$

$$\begin{aligned}
\int_{\mathcal{R}^D} abH(-\phi_a)\delta(\phi_p)\frac{\nabla\phi_p}{|\nabla\phi_p|}\cdot\nabla\frac{\partial\phi_a}{\partial\tau}H(-\phi_w) d\mathbf{r} &= -\int_{\mathcal{R}^D}\frac{\partial\phi_p}{\partial\tau}\nabla\cdot\left(abH(-\phi_a)\delta(\phi_p)\frac{\nabla\phi_p}{|\nabla\phi_p|}H(-\phi_w)\right) d\mathbf{r} \\
&= -\int_{\mathcal{R}^D}\frac{\partial\phi_p}{\partial\tau}\left(H(-\phi_a)\delta(\phi_p)H(-\phi_w)\left(\nabla\cdot\frac{\nabla\phi_p}{|\nabla\phi_p|}+\frac{\nabla\phi_p}{|\nabla\phi_p|}\cdot\nabla\right)(ab)\right. \\
&\quad \left.+abH(-\phi_a)\delta'(\phi_p)|\nabla\phi_p|H(-\phi_w)\right. \\
&\quad \left.-ab\delta(-\phi_a)\nabla\phi_a\cdot\frac{\nabla\phi_p}{|\nabla\phi_p|}\delta(\phi_p)H(-\phi_w)-abH(-\phi_a)\delta(\phi_p)\delta(-\phi_w)\nabla\phi_w\cdot\frac{\nabla\phi_p}{|\nabla\phi_p|}\right) d\mathbf{r} \\
&= -\int_{\mathcal{R}^D}\frac{\partial\phi_p}{\partial\tau}\left(H(-\phi_a)\delta(\phi_p)H(-\phi_w)\left(\nabla\cdot\frac{\nabla\phi_p}{|\nabla\phi_p|}+\frac{\nabla\phi_p}{|\nabla\phi_p|}\cdot\nabla\right)(ab)\right. \\
&\quad \left.+abH(-\phi_a)\delta'(\phi_p)|\nabla\phi_p|H(-\phi_w)\right) d\mathbf{r}.
\end{aligned}$$

$$\begin{aligned}
\int_{\mathcal{R}^D} ac\delta(\phi_w) \frac{\nabla\phi_w}{|\nabla\phi_w|} \cdot \nabla \frac{\partial\phi_w}{\partial\tau} H(-\phi_p)H(-\phi_a) d\mathbf{r} &= - \int_{\mathcal{R}^D} \frac{\partial\phi_w}{\partial\tau} \nabla \cdot \left(ac\delta(\phi_w) \frac{\nabla\phi_w}{|\nabla\phi_w|} H(-\phi_p)H(-\phi_a) \right) d\mathbf{r} \\
&= - \int_{\mathcal{R}^D} \frac{\partial\phi_w}{\partial\tau} \left(\delta(\phi_w)H(-\phi_p)H(-\phi_a) \left(\nabla \cdot \frac{\nabla\phi_w}{|\nabla\phi_w|} + \frac{\nabla\phi_w}{|\nabla\phi_w|} \cdot \nabla \right) ac \right. \\
&\quad \left. + ac\delta'(\phi_w) |\nabla\phi_w| H(-\phi_p)H(-\phi_a) \right. \\
&\quad \left. - ac\delta(\phi_w)\delta(-\phi_p)\nabla\phi_p \cdot \frac{\nabla\phi_w}{|\nabla\phi_w|} H(-\phi_a) - ac\delta(\phi_w)H(-\phi_p)\delta(-\phi_a)\nabla\phi_a \cdot \frac{\nabla\phi_w}{|\nabla\phi_w|} \right) d\mathbf{r} \\
&= - \int_{\mathcal{R}^D} \frac{\partial\phi_w}{\partial\tau} \left(\delta(\phi_w)H(-\phi_p)H(-\phi_a) \left(\nabla \cdot \frac{\nabla\phi_w}{|\nabla\phi_w|} + \frac{\nabla\phi_w}{|\nabla\phi_w|} \cdot \nabla \right) ac \right. \\
&\quad \left. + ac\delta'(\phi_w) |\nabla\phi_w| H(-\phi_p)H(-\phi_a) - ac\delta(\phi_w)H(-\phi_p)\delta(-\phi_a)\nabla\phi_a \cdot \frac{\nabla\phi_w}{|\nabla\phi_w|} \right) d\mathbf{r}.
\end{aligned}$$

Substituting the above expression into (33), using advection equation (28) and the fact that the normal vectors and curvatures of boundaries of Ω_a , Ω_p , and Ω_w are equal to

$$\begin{aligned}
\mathbf{n}_a &= \frac{\nabla\phi_a}{|\nabla\phi_a|}, & \kappa_a &= \nabla \cdot \left(\frac{\nabla\phi_a}{|\nabla\phi_a|} \right), \\
\mathbf{n}_p &= \frac{\nabla\phi_p}{|\nabla\phi_p|}, & \kappa_p &= \nabla \cdot \left(\frac{\nabla\phi_p}{|\nabla\phi_p|} \right), \\
\mathbf{n}_w &= \frac{\nabla\phi_w}{|\nabla\phi_w|}, & \kappa_w &= \nabla \cdot \left(\frac{\nabla\phi_w}{|\nabla\phi_w|} \right),
\end{aligned}$$

results in the following formulas

$$\begin{aligned}
\frac{\partial}{\partial \tau} \int_{\Omega} a \, d\mathbf{r} &= \int_{\mathcal{R}^D} a v_{\mathbf{n}} \delta(\phi_a) |\nabla \phi_a| H(-\phi_p) H(-\phi_w) \, d\mathbf{r} \\
&+ \int_{\mathcal{R}^D} a (\mathbf{v}_p - \boldsymbol{\omega}_p \times \mathbf{r}) \cdot \mathbf{n}_p H(-\phi_a) \delta(\phi_p) |\nabla \phi_p| H(-\phi_w) \, d\mathbf{r} \\
&+ \int_{\mathcal{R}^D} a (\mathbf{v}_w - \boldsymbol{\omega}_w \times \mathbf{r}) \cdot \mathbf{n}_w H(-\phi_a) H(-\phi_p) \delta(\phi_w) |\nabla \phi_w| \, d\mathbf{r}, \\
\frac{\partial}{\partial \tau} \int_{\Gamma_a} a \, d\mathbf{r} &= \int_{\mathcal{R}^D} v_{\mathbf{n}} \delta(\phi_a) |\nabla \phi_a| H(-\phi_p) H(-\phi_w) (\kappa + \partial_{\mathbf{n}}) a \, d\mathbf{r} \\
&+ \int_{\mathcal{R}^D} [(\mathbf{v}_w - \boldsymbol{\omega}_w \times \mathbf{r}) \cdot \mathbf{n}_w - v_{\mathbf{n}} \mathbf{n}_w \cdot \mathbf{n}_a] a \delta(\phi_a) |\nabla \phi_a| H(-\phi_p) \delta(-\phi_w) |\nabla \phi_w| \, d\mathbf{r}, \\
\frac{\partial}{\partial \tau} \int_{\Gamma_p} ab(\tau) \, d\mathbf{r} &= \int_{\mathcal{R}^D} (\mathbf{v}_p - \boldsymbol{\omega}_p \times \mathbf{r}) \cdot \left[a \nabla b + \mathbf{n}_p (\kappa + \partial_{\mathbf{n}}) (ab) \right] H(-\phi_a) \delta(\phi_p) |\nabla \phi_p| H(-\phi_w) \, d\mathbf{r}, \\
\frac{\partial}{\partial \tau} \int_{\Gamma_w} ac(\tau) \, d\mathbf{r} &= \int_{\mathcal{R}^D} ac (v_{\mathbf{n}} - (\mathbf{v}_w - \boldsymbol{\omega}_w \times \mathbf{r}) \cdot \mathbf{n}_w \mathbf{n}_w \cdot \mathbf{n}_a) \delta(\phi_a) |\nabla \phi_a| H(-\phi_p) \delta(\phi_w) |\nabla \phi_w| \, d\mathbf{r} \\
&+ \int_{\mathcal{R}^D} (\mathbf{v}_w - \boldsymbol{\omega}_w \times \mathbf{r}) \cdot \left[a \nabla c + \mathbf{n}_w (\kappa + \partial_{\mathbf{n}}) (ac) \right] H(-\phi_a) H(-\phi_p) \delta(\phi_w) |\nabla \phi_w| \, d\mathbf{r},
\end{aligned}$$

which after applying the coarea formulas and converting integrals into more traditional notation become (20). Note that these expressions contain integrals over the intersection of boundaries of Ω_a and Ω_w . These terms can be interpreted as additional surface generation as the boundary of Ω_a travels along the boundary of Ω_w (see figure 25).

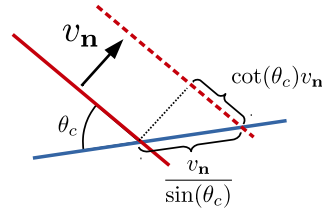


Figure 25: Interpretation of resulting expression for shape derivatives in case of sharp features.